8-15-2022

Attributing differences of solar-induced chlorophyll fluorescence (SIF)-gross primary production (GPP) relationships between two C4 crops: corn and miscanthus

Genghong Wu
University of Illinois Urbana-Champaign

Kaiyu Guan
University of Illinois Urbana-Champaign

Chongya Jiang
University of Illinois Urbana-Champaign

Hyungsuk Kimm
University of Illinois Urbana-Champaign

Guofang Miao
University of Illinois Urbana-Champaign

See next page for additional authors

Agricultural and Forest Meteorology 323 (2022) 109046

Contents lists available at ScienceDirect

Agricultural and Forest Meteorology

journal homepage: www.elsevier.com/locate/agrformet

Attributing differences of solar-induced chlorophyll fluorescence (SIF)-gross primary production (GPP) relationships between two C4 crops: corn and miscanthus

Genghong Wu [a,b,c,*], Kaiyu Guan [a,b,c,e,*], Chongya Jiang [a,b,c], Hyungsuk Kimm [a,b,d], Guofang Miao [b], Carl J. Bernacchi [a,c,f,h], Caitlin E. Moore [a,c,g], Elizabeth A. Ainsworth [a,c,f,h], Xi Yang [i], Joseph A. Berry [j], Christian Frankenberg [k,l], Min Chen [m,n]

[a] Agroecosystem Sustainability Center, Institute for Sustainability, Energy, and Environment, University of Illinois at Urbana Champaign, Urbana, IL 61801, USA
[b] Department of Natural Resources and Environmental Sciences, College of Agricultural, Consumers, and Environmental Sciences, University of Illinois, Urbana, IL 61801, USA
[c] DOE Center for Advanced Bioenergy and Bioproducts Innovation, Urbana, IL 61801, USA
[d] Department of Agriculture, Forestry, and Bioresources, College of Agriculture and Life Sciences, Seoul National University, Seoul 08826, KOR
[e] National Center for Supercomputing Applications, University of Illinois, Urbana, IL 61801, USA
[f] Department of Plant Biology, University of Illinois, Urbana, IL 61801, USA
[g] School of Agriculture and Environment, University of Western Australia, Crawley, WA 6009, AUS
[h] USDA-ARS, Global Change and Photosynthesis Research Unit, Urbana, IL 61801, USA
[i] Department of Environmental Sciences, University of Virginia, Charlottesville, VA 22903, USA
[j] Department of Global Ecology, Carnegie Institution for Science, Stanford, CA 94305, USA
[k] Division of Geological and Planetary Sciences, California Institute of Technology, Pasadena, CA 91125, USA
[l] Jet Propulsion Laboratory, California Institute of Technology, Pasadena, CA 91125, USA
[m] Department of Forest and Wildlife Ecology, University of Wisconsin-Madison, Madison, WI 53706, USA
[n] Nelson Institute Center for Climatic Research, University of Wisconsin-Madison, Madison, WI 53706, USA

ARTICLE INFO

Keywords:
C4 crops
Gross primary productivity
Leaf absorbed energy partition
Photosynthesis
Solar-induced chlorophyll fluorescence

ABSTRACT

There remains limited information to characterize the solar-induced chlorophyll fluorescence (SIF)-gross primary production (GPP) relationship in C4 cropping systems. The annual C4 crop corn and perennial C4 crop miscanthus differ in phenology, canopy structure and leaf physiology. Investigating the SIF-GPP relationships in these species could deepen our understanding of SIF-GPP relationships within C4 crops. Using in situ canopy SIF and GPP measurements for both species along with leaf-level measurements, we found considerable differences in the SIF-GPP relationships between corn and miscanthus, with a stronger SIF-GPP relationship and higher slope of SIF-GPP observed in corn compared to miscanthus. These differences were mainly caused by leaf physiology. For miscanthus, high non-photochemical quenching (NPQ) under high light, temperature and water vapor deficit (VPD) conditions caused a large decline of fluorescence yield (Φ_F), which further led to a SIF midday depression and weakened the SIF-GPP relationship. The larger slope in corn than miscanthus was mainly due to its higher GPP in mid-summer, largely attributed to the higher leaf photosynthesis and less NPQ. Our results demonstrated variation of the SIF-GPP relationship within C4 crops and highlighted the importance of leaf physiology in determining canopy SIF behaviors and SIF-GPP relationships.

1. Introduction

Accurate estimation of terrestrial gross primary production (GPP) is critical for quantifying the global carbon budget and understanding ecosystem responses to climate change (Ryu et al., 2019). Remote sensing of solar-induced chlorophyll fluorescence (SIF) has emerged as a new promising approach to estimate GPP at regional to global scales (Frankenberg et al., 2011; He et al., 2019; Mohammed et al., 2019). SIF, an optical signal emitted by plants in the spectral range of 650-850nm, provides a functional link with photosynthesis as, along with

* Corresponding authors.
E-mail addresses: gw8@illinois.edu (G. Wu), kaiyug@illinois.edu (K. Guan).

https://doi.org/10.1016/j.agrformet.2022.109046
Received 2 January 2022; Received in revised form 19 May 2022; Accepted 6 June 2022
Available online 21 June 2022

photochemistry and heat dissipation, it represents one of the three possible fates for absorbed light by leaf chlorophyll molecules (Baker, 2008; Porcar-Castell et al., 2014; Frankenberg and Berry, 2018). Current approaches that use satellite-derived SIF for global GPP estimation mainly include (1) directly using SIF to estimate GPP based on the site-scale SIF-GPP relationships (Li and Xiao, 2019; Wang et al., 2020; Zhang et al., 2020a, b; Liu et al., 2022a), or (2) assimilating SIF into land surface models to improve GPP estimations (Thum et al., 2017; MacBean et al., 2018; Norton et al., 2019). Both approaches analyze the SIF-GPP relationship based on plant functional types (PFTs) without considering variation within a PFT. For example, initially, estimation of crop GPP from satellite SIF was achieved by building a universal relationship between satellite SIF and eddy covariance-based GPP for available cropland sites, which was used to generate regional-scale crop GPP estimates (Guanter et al., 2014). More recent work has differentiated C3 and C4 crops, and built the SIF-GPP relationship separately (Zhang et al., 2020a; Li and Xiao, 2022) by using increased spatial resolution satellite SIF products (Sun et al., 2017; Wen et al., 2020). Yet, variation of SIF-GPP relationships within C3 and/or C4 crops is largely unknown.

Understanding of SIF-GPP relationships at the ecosystem scale is improving for C3 crops from fine spatiotemporal in situ spectral measurements in soybean (Miao et al., 2018), rice (Yang et al., 2018a) and wheat (Goulas et al., 2017). Variation in SIF-GPP relationships within C3 crops can be found in previous studies (Yang et al., 2018a; He et al., 2020). For example, a non-linear SIF-GPP relationship at half-hourly timestep was reported in soybean in He et al. (2020), but a linear and stronger SIF-GPP relationship was found in rice (Yang et al., 2018a). However, C4 crop understanding remains limited to corn (He et al., 2020; Li et al., 2020; Miao et al., 2020; Yang et al., 2021). Continuous canopy SIF and GPP measurements from other C4 crops are needed to understand the variation of SIF-GPP relationships within C4 crops.

SIF-GPP relationships depend on a number of factors, including canopy structure (Migliavacca et al., 2017; Dechant et al., 2020), leaf physiology (Celesti et al., 2018; Magney et al., 2019),environmental conditions (Verma et al., 2017; Paul-Limoges et al., 2018; Chen et al., 2021b, a), and sun-view geometry (Hao et al., 2021; Zhang et al., 2021). The role of these factors in affecting SIF-GPP relationships can be well explained when both SIF and GPP are conceptually described by the light use efficiency framework (Monteith, 1972). For GPP, we have

$$GPP = FPAR \times PAR \times LUE \quad (1)$$

Where PAR is the incoming photosynthetic active radiation, FPAR is the fraction of absorbed PAR of the canopy, and LUE is the photosynthetic light use efficiency of the canopy. Similarly, for observed canopy SIF, we have:

$$SIF = FPAR \times PAR \times SIFy \quad (2)$$

where SIFy is the apparent SIF yield which is the effective light use efficiency of canopy fluorescence. SIFy can be further quantified by the product of the true fluorescence yield of the whole canopy ($\Phi_{F,\ Canopy}$) and the escape probability (f_{esc}) of SIF from the canopy since the multi-scattering and absorption process within the canopy causes that only a fraction of SIF emitted by all leaves can be observed from top of the canopy (Romero et al., 2018; Yang and van der Tol, 2018). Canopy structure such as leaf area index (LAI) and the leaf clumping effect affects FPAR (Baret and Guyot, 1991) and f_{esc} (He et al., 2017; Yang and van der Tol, 2018). Leaf physiology impacts LUE and $\Phi_{F,\ Canopy}$, which further strongly depends on the energy partitioning of absorbed PAR (APAR) into photochemistry, fluorescence and heat dissipation during the light reactions of photosynthesis at the leaf level (Porcar-Castell et al., 2014; Gu et al., 2019a). Additionally, environmental conditions would substantially affect the energy partitioning of APAR (Flexas and Medrano, 2002), since plants tend to maximize APAR for photochemistry under optimal environmental conditions, but less ideal environmental conditions (e.g., suboptimal temperature, moisture and light) reduce photochemistry (Ač et al., 2015), and fluorescence and non-photochemical quenching (NPQ) compete to de-excite the APAR that is not used in photochemistry (Porcar-Castell et al., 2014).

Both corn and miscanthus are important C4 bioenergy crops (Robertson et al., 2017). The annual crop corn (Zea mays) is a popular feedstock for ethanol production attributed to its abundance, high starch content in grains and easy conversion to ethanol (Mumm et al., 2015). Giant miscanthus (Miscanthus x giganteus) is a warm-season, perennial grass, and it plays important roles in bioenergy production with its high biomass production (Heaton et al., 2010), high nutrient-use efficiencies (Smith et al., 2013) and high energy output/input (Felten et al., 2013). Compared to corn, miscanthus can develop leaves earlier and maintain them longer (Beale and Long, 1995). Side-by-side trials have found higher biomass in miscanthus compared to corn, which is largely due to more green leaves (higher green LAI) and a longer growing season, although the maximum leaf and canopy photosynthesis of miscanthus under favorable conditions are lower than corn (Dohleman and Long, 2009; Moore et al., 2021). Higher LAI in miscanthus would result in higher FPAR when FPAR is not saturated (Gallo et al., 1985), and it might also lead to more far-red SIF photons escaping from the canopy since higher LAI is expected to increase f_{esc} (Yang and van der Tol, 2018). Higher corn canopy LUE compared to miscanthus during mid-summer has been found in side-by-side field-grown plots, resulting in higher GPP in corn than that in miscanthus during mid-summer (Moore et al., 2021). Leaf-level measurements have also shown that midday photochemical yield (Φ_P), midday electron transport rate (ETR) and maximum quantum yield for CO_2 assimilation ($\Phi_{CO2,\ max}$) are higher in corn compared to miscanthus (Dohleman and Long, 2009), indicating that the energy partitioning of leaf APAR might be different between corn and miscanthus. For corn, more leaf APAR tends to be used for photochemistry and further CO_2 assimilation and less APAR for fluorescence and heat dissipation compared to miscanthus. This different energy partitioning might cause different SIF-GPP relationships between corn and miscanthus. Additionally, miscanthus can maintain photosynthesis at lower temperatures than corn (Dohleman and Long, 2009) and the optimum temperature for light saturated photosynthesis is lower in miscanthus compared to corn (Naidu and Long, 2004), indicating that the photosynthesis response to environmental conditions might be different between miscanthus and corn. All these differences in canopy structure, leaf physiology and environmental responses could possibly cause variations of SIF-GPP relationships between corn and miscanthus. Comparing the SIF-GPP relationships between corn and miscanthus can help us better understand the variation of SIF-GPP relationships within C4 crops.

In this study, we attempt to determine whether the SIF-GPP relationship differs between two contrasting C4 cropping systems, annual corn and perennial miscanthus. To comprehensively assess their relationships, we integrated canopy SIF, eddy covariance flux measurements, meteorological variables along with leaf-level active fluorescence measurements using the pulse amplitude modulation (PAM) technique. Specifically, we propose the following questions: (1) Does the SIF-GPP relationship vary between an annual C4 corn system and a perennial C4 miscanthus system? (2) How do the growing season climate conditions affect the seasonal and diurnal SIF-GPP relationships in corn and miscanthus? (3) How do the growing season climate conditions affect canopy LUE and SIFy as well as leaf Φ_P and fluorescence yield ($\Phi_{F,\ Leaf}$) in corn and miscanthus?

2. Data and methods

2.1. Study sites

This study was conducted at the Energy Farm of University of Illinois at Urbana-Champaign (UIUC) located in the Midwest of the U.S. The regional climate is characterized as hot summers and cold winters. The

mean annual precipitation was 928 mm, and mean annual temperature was 11.3°C with winter monthly minimum -13.1°C and summer monthly maximum 33.9°C over the period of 2000–2020 (University of Illinois Willard Airport weather station). The miscanthus (*Miscanthus* × *giganteus*) site and corn (*Zea mays*) site were next to each other, and both of them were established in 2008 (Fig. S1). The corn site (40.06284°N, -88.19612°W) was implemented with corn-corn-soybean rotation, and the miscanthus site (40.06285°N, -88.19842°W) was only planted with perennial miscanthus. As an annual crop, corn was planted in May and harvested in October each year. As a perennial crop, miscanthus emerged in April and was harvested in March the following year after establishment in May 2008. Both sites were rainfed sites and sufficient fertilizers were applied at both sites. Soil in these two sites were composed of primarily Dana silt loams, Flanagan silt loams, and Drummer silty clay loams (Moore et al., 2021). Spectral systems for SIF data collection were installed in 2018 at the corn site, and in 2019 and 2020 at the miscanthus site. For the corn site in 2018, 202 kg ha^{-1} 32% UAN were applied on 8th May and corn was planted in the east-west orientation (Fig. S2). Corn started to tassel around 4th July in 2018 and bottom corn leaves started to turn yellow in late August (Fig. S3). For the miscanthus site in 2019 and 2020, 56 kg ha^{-1} granular urea N were applied on 21st June and 12th June, respectively. Previous studies revealed that adding more N in the same miscanthus site did not further increase biomass (Lee et al., 2017), so this site did not have nutrient stress. As an annual grass with natural emergence, miscanthus had no row pattern (Fig. S2). Miscanthus started to flower at the end of September in both 2019 and 2020 (Fig. S3). To account for the different growing season lengths of corn and miscanthus, only data from July and August when both canopies were fully closed were used in this study.

2.2. Tower-based spectral measurements

Fluospec2 systems (Miao et al., 2018; Yang et al., 2018b) were installed at the two sites to collect spectral data. Each Fluospec2 consisted of two subsystems. One subsystem was for SIF data collection where a QE Pro spectrometer with a spectral resolution 0.15 nm and wavelength coverage between 730 and 780 nm (Ocean Optics Inc., Dunedin, FL, USA) was employed. The other subsystem was for hyperspectral data collection which was equipped with a HR2000+ spectrometer (Ocean Optics Inc.) covering the wavelength between 400 and 1100 nm with a 1.1 nm spectral resolution. Each subsystem has two channels to measure downwelling solar irradiance (E) and upwelling canopy reflected radiance (L) simultaneously. The upward viewing fibers for solar irradiance were equipped with a cosine corrector to enable a hemispherical observation, while downward nadir-view observations for canopy radiance used bare fibers with a field of view (FOV) of 25°. All fibers were placed 5 m above the ground pointing to the south. Data was acquired by the software FluoSpec Manager which dynamically set optimized integration times at a 5-min time interval (Yang et al., 2018b). SIF at 760 nm (SIF_{760}) was retrieved from measured irradiance and radiance of the SIF subsystem using the improved Fraunhofer Line Depth (iFLD) approach (Alonso et al., 2008; Cendrero-Mateo et al., 2019). This retrieval method decoupled fluorescence from the reflected radiance using the E and L information from 745–780 nm. Raw 5-min SIF_{760} data was averaged to a half-hourly interval to match the GPP data. Detailed information about the Fluspec2 measurement sequence and SIF retrieval can be found in Wu et al. (2020).

2.3. Eddy covariance flux and environmental measurements

Eddy-covariance (EC) towers were established in the same field as the Fluospec2 systems to measure ecosystem carbon flux which was further used for GPP estimation for corn and miscanthus. Each EC system was composed of an open path infrared gas analyzer (LI-7500RS; LICOR Biosciences, Lincoln, NE, USA) for CO_2 concentration and a three-dimensional ultrasonic anemometer (81000RE; RM Young) for wind speed and direction measurements. EC measurements were recorded at 10 Hz frequency and were processed to acquire half-hourly average net ecosystem exchange (NEE) using EddyPro (v6.2.0; LICOR Biosciences). EddyPro applied block averaging for flux de-trending, double rotation for instrument tilt correction, covariance maximization for time-lag compensation, Webb−Pearman−Leuning flux density correction (Webb et al., 1980), spikes detection and removal (Vickers and Mahrt, 1997), and a footprint calculation (Hsieh et al., 2000). EddyPro processed half-hourly NEE were quality assured and quality controlled (QA/QC) to remove spikes and outliers. Footprint filter was also applied to remove data when more than 50% of the data occurred outside of the targeted field. Friction velocity threshold filter was further applied to remove data collected under low turbulent mixing conditions.

Climate variables were measured along with the EC measurements. Air temperature (Ta) and relative humidity (RH) were measured using a combined probe (HMP-45C & 43347-IX; Campbell Scientific, Logan, UT, USA), from which water vapor deficit (VPD) was calculated. Incoming PAR was measured using a point quantum sensor (LI-190; LICOR Biosciences). Soil water content (SWC) was measured at 10 cm depth (Hydra Probe II; Stevens Water Monitoring Systems). The meteorological data were further gap-filled with external data from the University of Illinois Willard Airport weather station (7.4 km away) and ERA5 data from the European Centre for Medium Range Forecasts. Both the EC system and aboveground meteorological instruments were installed 2.5 m above the ground at the beginning of the growing season, and height was increased to be around 1 m above the canopy with the growth of crops. Detailed EC and meteorological instrumentations can be found in Moore et al. (2021).

Filtered NEE data were gap-filled along with the gap-filled incoming radiation, Ta, and VPD using the Marginal Distribution Sampling (MDS) method described in Reichstein et al. (2005). Gap-filled NEE were then partitioned into GPP and ecosystem respiration (ER) using both standard nighttime fluxes method (Reichstein et al., 2005) and daytime fluxes method (Lasslop et al., 2010). For the nighttime method, nighttime NEE was used to develop an ER-temperature model and this model was used to estimate daytime ER. GPP was calculated as the difference between ER and NEE. Windows of 14 days were applied to parameterize the ER model in order to account for the dynamic of other drivers of ER. For the daytime method, daytime data was used to parameterize a model for GPP based on a light response curve and VPD, and nighttime data was used to build the ER-temperature model for ER estimation. Windows of 8 days were applied to parameterize the models. We used the open source ONEFlux processing pipeline to estimate both nighttime method partitioned GPP (GPP_{NT}) and daytime method partitioned GPP (GPP_{DT}) from EC measurements (Pastorello et al., 2020). GPP_{NT} and GPP_{DT} are strongly correlated (R^2=0.77–0.83) in the three year-sites (Fig. S4). Since GPP_{DT} considered the impacts of PAR and VPD on GPP at the diurnal scale, we used GPP_{DT} in the main text and GPP_{NT} in the supplementary materials. For simplicity, GPP was used for GPP_{DT} in the main text.

2.4. Correcting in situ nadir SIF to EC footprint-based SIF

EC footprint coves a larger area compared to nadir-view SIF observations (Liu et al., 2017) and it changes with wind direction (Kljun et al., 2015), which may bring uncertainty when comparing the SIF-GPP relationships between corn and miscanthus. To address this SIF and GPP footprint mismatch issue, the product of near-infrared reflectance of vegetation (NIRv) and PAR (NIRvP) was used as a proxy for SIF to upscale in situ SIF observations from small nadir footprints to large EC footprints to match the GPP estimates, considering that NIRvP can explain around 80% variation of SIF from recent cross-scale studies (Kimm et al., 2021; Dechant et al., 2022). Daily NIRv was calculated from gap-free surface reflectance obtained through PlanetScope surface reflectance product after radiometric correction and temporal filtering (detailed information can be found in supplementary materials).

Soil-adjusted NIRv (SANIRv) was further calculated following the method in Jiang et al. (2020) to eliminate the soil background impact on NIRv, and was used to correct SIF footprint. We assumed no diurnal variations of SANIRv and all half-hourly SANIRv within one day was the same as the daily SANIRv of that day. SIF footprint (about 3.8 m^2) was represented by a single 3m × 3m pixel of PlanetScope imagery covering the SIF tower. Half-hourly EC footprint was calculated using the Simple Analytical Footprint model on Eulerian coordinates (SAFE) model with the inputs of meteorological variables and fluxes, including half-hourly air temperature, relative humidity, air pressure, wind speed, wind direction, standard deviation of the transverse wind speed, friction velocity, sensible heat flux, latent heat flux and NEE (Chen et al., 2009). EC footprint-based SIF at each half-hour ($SIF_{EC\ footprint}$) was calculated from in situ nadir-view SIF observations (SIF_{obs}) based on the following equations:

$$\begin{aligned} SIF_{EC\ footprint} &= SIF_{obs} \times Ratio \\ Ratio &= \frac{SANIRv_{EC\ footprint} \times PAR_{EC\ footprint}}{SANIRv_{SIF\ pixel} \times PAR_{SIF\ pixel}} \\ SANIRv_{EC\ footprint} &= \Sigma_{i=1}^{N} w_i \times SANIRv_i \end{aligned} \quad (3)$$

where ***Ratio*** is the ratio of the product of weighted SANIRv ($\boldsymbol{SANIRv_{EC\ footprint}}$) and PAR ($\boldsymbol{PAR_{EC\ footprint}}$) from EC footprint and the product of SANIRv ($\boldsymbol{SANIRv_{SIF\ pixel}}$) and PAR ($\boldsymbol{PAR_{SIF\ pixel}}$) from SIF tower located pixel at each half-hour. Without considering the PAR variation within each field (i.e. $\boldsymbol{PAR_{EC\ footprint} \approx PAR_{SIF\ piexl}}$), each half-hourly ratio can be calculated as $\boldsymbol{Ratio} = \frac{\boldsymbol{SANIRv_{EC\ footprint}}}{\boldsymbol{SANIRv_{SIF\ pixel}}}$. EC footprint weighted $\boldsymbol{SANIRv_{EC\ footprint}}$ was calculated by the sum of the product of SANIRv ($\boldsymbol{SANIRv_i}$) and footprint weight ($\boldsymbol{w_i}$) at each pixel i across all the pixels within the EC footprint N. The EC footprint in these three year-sites was constrained by the boundary of each target field with a size of 4 ha (200m × 200m, Fig. S5). The crop growth at 2018 corn and 2020 miscanthus sites was relatively homogenous in July and August indicated by the SANIRv map (Fig. S5), which caused ***Ratio*** of $\boldsymbol{SANIRv_{EC\ footprint}}$ to $\boldsymbol{SANIRv_{SIF\ pixel}}$ close to 1 (Fig. S6). Miscanthus in the west side of the 2019 miscanthus field had better growth compared to the east side, which led to ***Ratio*** values higher than 1 (Fig. S6). Corrected EC footprint-based SIF at the corn and miscanthus sites were used for later analysis, with the variable "SIF_{760}" for simplicity.

2.5. Derivation of canopy LUE, SIFy, f_{esc} and $\Phi_{F,\ Canopy}$

At the Miscanthus site, APAR was calculated from in situ PAR measurements. Incoming PAR (PAR_{in}) and surface reflected PAR (PAR_{out}) were measured using point quantum sensors (LI-190; LICOR Biosciences) pointing upward and downward at 5 m above the ground, respectively. Transmitted PAR through the canopy (PAR_{trans}) was measured using a line quantum sensor (LI-191; LICOR Biosciences) looking upward placed about 2 cm above the ground. Half-hourly APAR and the fraction of absorbed PAR (FPAR) can be calculated as:

$$\begin{aligned} PAR &= PAR_{in} - PAR_{out} - PAR_{trans} \\ FPAR &= \frac{APAR}{PAR_{in}} \end{aligned} \quad (4)$$

For the corn site, canopy FPAR was estimated by the normalized red-edge normalized difference vegetation index (Rededge NDVI) due to the missing PAR_{trans} measurment. This method has been used in many previous corn studies (Viña and Gitelson, 2005; Li et al., 2020; Yang et al., 2021). APAR was calculated as the product of PAR_{in} and estimated FPAR.

$$\begin{aligned} FPAR &= 1.37\ \times Rededge\ NDVI - 0.17 \\ Rededge\ NDVI &= \frac{R_{NIR} - R_{Red-edge}}{R_{NIR} - R_{Red-edge}} \\ APAR &= FPAR \times PAR_{in} \end{aligned} \quad (5)$$

where R_{NIR} and $R_{Red\text{-}edge}$ were the reflectance derived from spectral data collected by the broadband reflectance subsystem of the Fluospec2 system in bands of 750–757.5 nm and 703.75–713.75 nm, respectively. We note that the measured FPAR in miscanthus represented the total FPAR of the canopy while the estimated FPAR from Rededge NDVI in corn mainly represented the FPAR absorbed by green leaves. However, our study focused on July and August when canopies were mainly composed of green leaves, therefore, the differences between the two FPARs calculation were expected to be small. For both corn and miscanthus, the apparent SIF yield (SIFy) and LUE were derived as SIF/APAR and GPP/APAR, respectively. f_{esc} was quantified as the ratio of NIRv and FPAR (Zeng et al., 2019), and $\Phi_{F,\ Canopy}$ was calculated by dividing SIFy by f_{esc}:

$$\begin{aligned} f_{esc} &= \frac{\mathrm{NIRv}}{FPAR} \\ \Phi_{F,\ Canopy} &= \frac{SIFy}{f_{esc}} \end{aligned} \quad (6)$$

2.6. Leaf-level active chlorophyll fluorescence measurements

Light response curves of top sunlit leaves were measured using an LI-6800 portable photosynthesis system (LI-6800; LICOR Biosciences) with a leaf chamber fluorometer during mid-summer (i.e. July) to understand the leaf energy partitioning at different light levels. Except for changing PAR, other environmental variables were controlled, i.e., CO_2 concentration at 400 ppm; leaf temperature at 27°C; relative humidity at 55%. For each response curve, we first measured the minimum (F_0) and maximum fluorescence of the dark-adapted leaf (F_M) predawn. Then the same leaf was illuminated to different light levels. For each light level, the leaf was illuminated for 15 min until steady-state fluorescence (F_S), light-adapted minimum fluorescence (F_0') and maximum fluorescence (F_M') were recorded. The light levels used for the miscanthus light response curve were 12, 25, 75, 100, 150, 200, 300, 400, 550, 700, 900, 1200, 1500, 1800, 2000 and 2200 μmol m^{-2} s^{-1}. The light levels used for the corn light response curve were 12, 25, 75, 100, 125, 150, 200, 300, 400, 450, 500, 550, 600, 700, 800, 900, 1200, 1500, 1800 and 2200 μmol m^{-2} s^{-1}. One light response curve of a mature leaf at the top of the canopy was conducted on one day considering the time requirement (~4 hours). For corn, two curves were taken on July 17th and 18th of 2018 using the same LI-6800. For miscanthus, five curves from July to August in 2019 (July 6th, July 13th, July 28th, Aug 3rd, Aug 30th) were measured.

We also installed an automated Moni-PAM system (MONI-PAM; Walz Heinz GmbH) with four Moni-PAM emitter–detector probes at the miscanthus site in 2020 to collect continuous PAM-fluorescence. The four probes were positioned to measure sunlit leaves in the upper canopy. Continuous F_S, F_0' and F_M' were collected every half hour. Dark-adapted F_0 and F_M were recorded at 2:00 am each morning. Ambient PAR and leaf temperature (T_{Leaf}) were simultaneously recorded by the system at half-hourly timestep. Data from the Moni-PAM system collected from July to Aug of 2020 were used for later analysis.

For both LI-6800 and Moni-PAM measurements, leaf-level $\Phi_{F,\ Leaf}$, Φ_P, quantum yield of heat dissipation through NPQ (Φ_N), and quantum yield of constitutive heat dissipation (Φ_D) were estimated. $\Phi_{F,\ Leaf}$ was calculated based on expression proposed by Gu et al. (2019a):

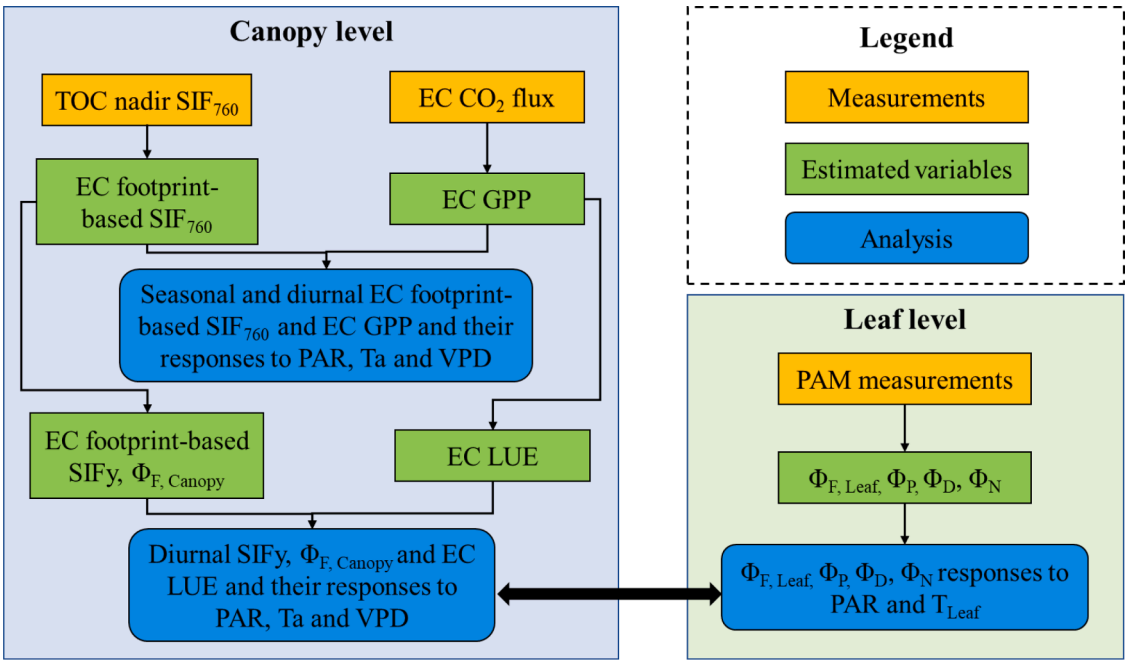

Fig. 1. Flowchart of measurements, estimated variables and analysis in each year-site. TOC: top of canopy; EC: eddy covariance. (For interpretation of the references to color in this figure legend, the reader is referred to the web version of this article.).

$$\Phi_{F,\ Leaf} = \frac{1-\phi_{P,\ max}}{(1+K_{DF})\left[(1+NPQ)\times\left(1-\Phi_{P,max}\right)+q_L\times\ \Phi_{P,max}\right]}$$
$$\Phi_{P,max} = 1-\frac{F_0}{F_M}$$
$$NPQ = \frac{F_M}{F_M'}-1 \quad (7)$$
$$q_L = \frac{F_M'-F_S}{F_M'-F_0'}\times\frac{F_0'}{F_S}$$

where $\Phi_{P,\ max}$ is the maximum photochemical yield calculated from the dark-adapted minimum and maximum fluorescence; NPQ quantifies the non-photochemical quenching heat dissipation process; q_L represents the fraction of photosystem II reaction centers with fully oxidized primary quinone electron acceptor; K_{DF} is the ratio of rate constant of constitutive heat dissipation (K_D) to rate constant of fluorescence emission (K_F), and assumed to be constant 19 (Gu et al., 2019a). Φ_P was calculated based on expression proposed by Genty et al. (1989):

$$\Phi_P = 1-\frac{F_S}{F_M'} \quad (8)$$

Φ_N was estimated using the equation proposed by Hendrickson et al. (2004):

$$\Phi_N = \frac{F_S}{F_M'}-\frac{F_S}{F_M} \quad (9)$$

Because of energy conservation, the sum of the four quantum yields is unity (Hendrickson et al., 2004). Therefore, Φ_D was calculated as:

$$\Phi_D = 1-\Phi_{F,\ Leaf}-\Phi_P-\Phi_N \quad (10)$$

2.7. Statistical analysis

To test our hypotheses, the relationships between SIF_{760} and GPP were investigated for corn and miscanthus. Linear regressions of GPP-SIF_{760} at half-hourly and daily scales were established for corn and miscanthus separately. Hyperbolic regression (Damm et al., 2015; Kim et al., 2021) and exponential regression (Liu et al., 2022b) of GPP-SIF_{760} were also applied to investigate the non-linearity of GPP-SIF_{760} in corn and miscanthus considering that GPP might saturate at higher APAR conditions but SIF would continue to increase with APAR. Regression equations and R^2 of the linear, hyperbolic and exponential regressions were compared between corn and miscanthus. Analysis of covariance (ANCOVA) was used to test whether SIF_{760}-GPP relationship between corn and miscanthus was significantly different. Considering the uncertainties of SIF_{760} under low light conditions, only data from 8:00 am to 6:00 pm (US central summer daylight time) were used. Daily data were averaged from 8:00 am to 6:00 pm half-hourly data when data gaps were less than 10%. Therefore, daily means represent daytime-only values. Sunny days were identified by the ratio of actual PAR to theoretical PAR calculated from dates and solar zenith angles (Weiss and Norman, 1985). The ratio at half-hourly scale was first calculated, and the half-hourly period was defined as sunny when the ratio was above 0.65. Sunny day was then defined when more than 75% of the half-hourly period between 8:00 am to 6:00 pm was sunny. *r* and partial correlation coefficients (ρ) were computed to measure the response of SIF_{760}, GPP, leaf and canopy light use efficiency to each environmental variable, i.e., PAR, Ta and VPD. When computing ρ between SIF_{760} or GPP and one environmental variable, the other two environmental variables were controlled. All the measurements, estimated variables and analysis were summarized in Fig. 1.

3. Results

3.1. Seasonal variations of environmental conditions, SIF_{760} and GPP

Miscanthus site in 2019 experienced slightly hotter and drier conditions compared to corn site in 2018 (Fig. 2). Daily Ta ranged from 17.76°C to 30.69°C with mean 25.85°C in 2018 corn, from 21.13°C to 31.34°C with mean 26.32°C in 2019 miscanthus and from 19.76°C to 30.72°C with mean 26.70°C in 2020 miscanthus. Daily VPD varied from 1.68 hPa to 16.95 hPa with mean 10.57 hPa in 2018 corn, from 5.26 hPa to 18.30 hPa with mean 12.23 hPa in 2019 miscanthus and from 2.04 hPa to 21.46 hPa with mean 12.74 hPa in 2020 miscanthus. Daily SWC at 10 cm varied from 0.20 $m^3\ m^{-3}$ to 0.36 $m^3\ m^{-3}$ in corn and from 0.19 $m^3\ m^{-3}$ to 0.39 $m^3\ m^{-3}$ in miscanthus. Overall, both corn and

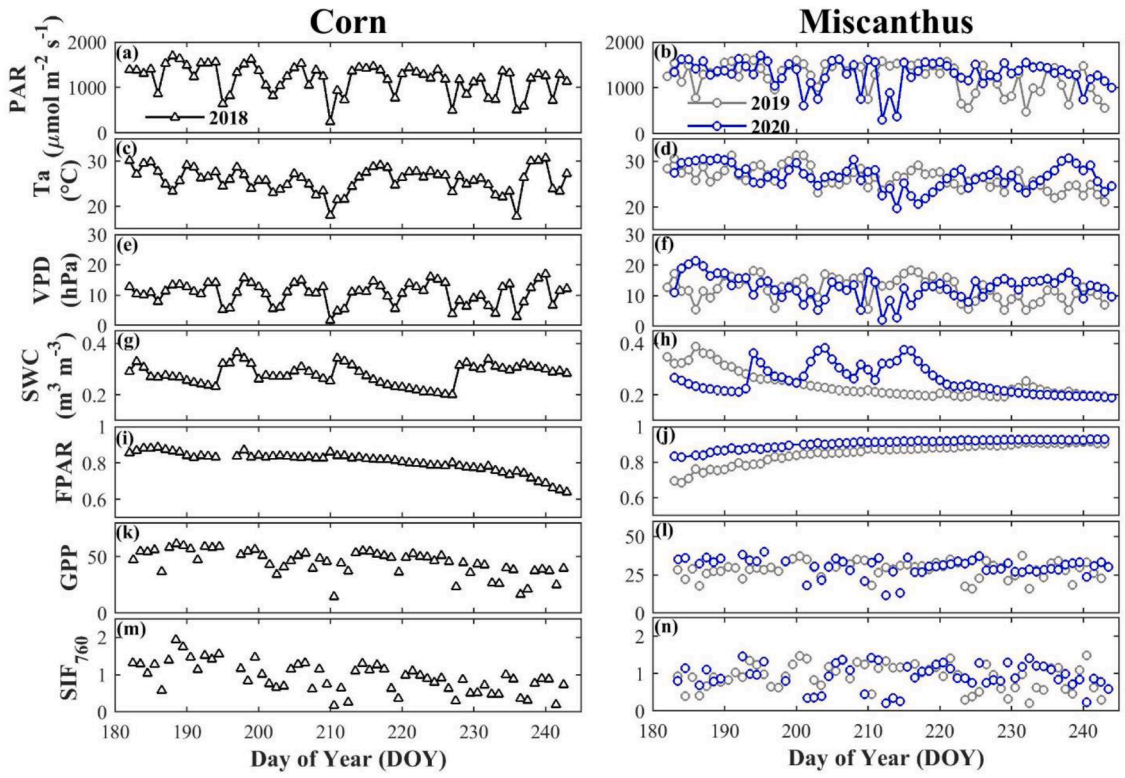

Fig. 2. Variation of daytime mean environmental variables, NDVI, GPP and SIF_{760} for corn (left) and miscanthus (right). Time series of daily (a and b) incoming photosynthetic active radiation (PAR, μmol m^{-2} s^{-1}), (c and d) air temperature (Ta,°C), (e and f) vapor pressure deficit (VPD, hPa), (g and h) volumetric soil water content at 10 cm (SWC, m^3 m^{-3}), (i and j) fraction of absorbed PAR (FPAR), (k and l) gross primary production (GPP, μmol m^{-2} s^{-1}) and (m and n) far-red solar-induced chlorophyll fluorescence (SIF_{760}, mW m^{-2} nm^{-1} sr^{-1}). Corn data were from 2018 (black triangles). Miscanthus data were from 2019 (grey circles) and 2020 (blue circles). All data were daily means from 8:00 am to 6:00 pm. (For interpretation of the references to color in this figure legend, the reader is referred to the web version of this article.).

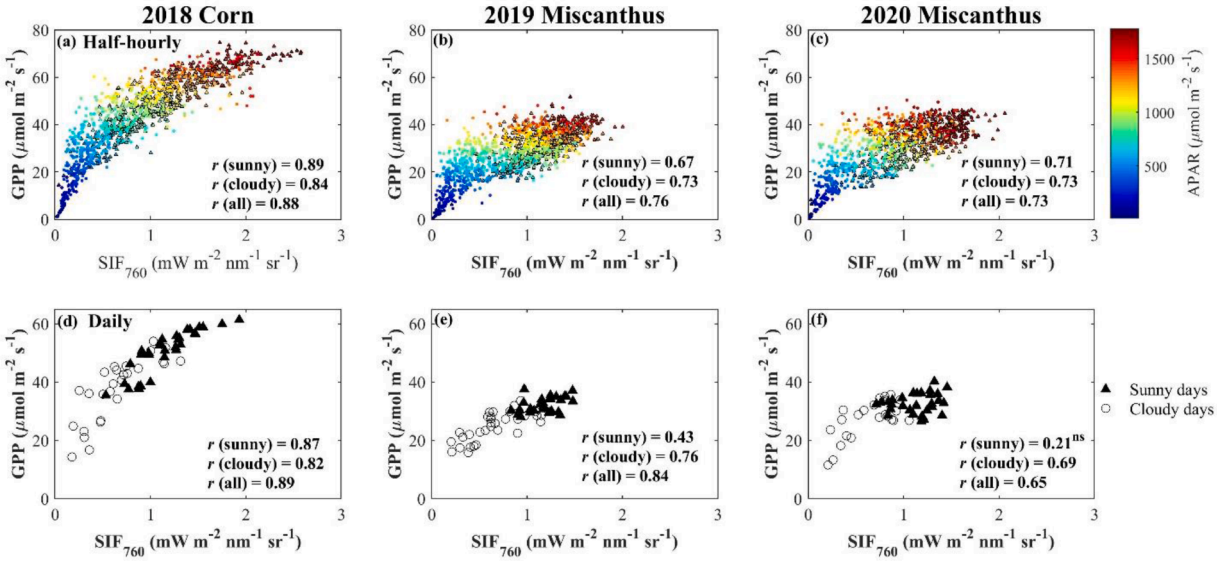

Fig. 3. Relationships between canopy SIF_{760} and GPP at half-hourly and daily scales in (a and d) 2018 corn, (b and e) 2019 miscanthus and (c and f) 2020 miscanthus. Half-hourly SIF_{760}-GPP relationships were colored by APAR, and the colored triangles with black edge color were sunny days and the colored circles were cloudy days. Daily SIF_{760}-GPP relationships were separated into sunny days (white circles) and cloudy days (black triangles). "ns" indicated that SIF_{760} and GPP were not significantly correlated. Other *r* values were statistically significant. (For interpretation of the references to color in this figure legend, the reader is referred to the web version of this article.).

miscanthus were not severely water stressed during the two growing seasons since the crop wilting point at this region was typically 0.14 m^3 m^{-3} (Illinois State Water Survey, 2020).

Overall, SIF_{760} and GPP followed similar seasonal patterns in both species with larger day-to-day variations observed in SIF_{760} (Fig. 2). Average daily GPP and SIF_{760} from July to August were higher for corn

Table 1
Equations and R^2 for SIF_{760}-GPP relationships using different fitting functions in corn and miscanthus dataset at half-hourly and daily scales.

Time scale	Model	Fitted Equation			R^2		
		2018 Corn	2019 Miscanthus	2020 Miscanthus	2018 Corn	2019 Miscanthus	2020 Miscanthus
Half- hourly	Linear without intercept	$y=41.95x$	$y=28.32x$	$y=29.83x$	0.77	0.69	0.67
	Linear	$y=25.31x+21.09$	$y=16.02x+13.93$	$y=15.99x+15.75$	0.77	0.57	0.53
	Hyperbolic	$y=\frac{85.04x}{(x+0.67)}$	$y=\frac{44.53x}{(x+0.40)}$	$y=\frac{47.49x}{(x+0.41)}$	0.83	0.61	0.57
	Exponential	$y=65.19(1-e^{-1.59x})$	$y=35.56(1-e^{-2.39x})$	$y=37.96(1-e^{-2.31x})$	0.82	0.59	0.56
Daily	Linear without intercept	$y=44.39x$	$y=29.11x$	$y=30.67x$	0.77	0.71	0.62
	Linear	$y=24.64x+21.71$	$y=13.00x+16.63$	$y=10.94x+20.39$	0.79	0.70	0.42
	Hyperbolic	$y=\frac{82.70x}{(x+0.71)}$	$y=\frac{42.51x}{(x+0.40)}$	$y=\frac{40.73x}{(x+0.27)}$	0.82	0.72	0.55
	Exponential	$y=62.51(1-e^{-1.59x})$	$y=33.74(1-e^{-2.42x})$	$y=33.65(1-e^{-3.22x})$	0.81	0.70	0.57

Table 2
Equations and R^2 for SIF_{760}-GPP relationships using different regression functions on sunny days and cloudy days in corn and miscanthus dataset at half-hourly scale.

Time scale	Model	Fitted Equation			R^2		
		2018 Corn	2019 Miscanthus	2020 Miscanthus	2018 Corn	2019 Miscanthus	2020 Miscanthus
Sunny days	Linear without intercept	$y=40.00x$	$y=26.68x$	$y=27.65x$	0.77	0.62	0.66
	Linear	$y=22.47x+24.27$	$y=15.66x+13.83$	$y=15.94x+14.66$	0.79	0.44	0.51
	Hyperbolic	$y=\frac{99.50x}{(x+1.02)}$	$y=\frac{67.17x}{(x+1.23)}$	$y=\frac{60.33x}{(x+0.89)}$	0.82	0.45	0.53
	Exponential	$y=72.82(1-e^{-1.14x})$	$y=46.88(1-e^{-1.03x})$	$y=44.31(1-e^{-1.28x})$	0.81	0.45	0.53
Cloudy days	Linear without intercept	$y=47.27x$	$y=31.63x$	$y=36.43x$	0.73	0.66	0.67
	Linear	$y=28.98x+18.83$	$y=17.37x+13.47$	$y=20.31x+14.38$	0.70	0.53	0.54
	Hyperbolic	$y=\frac{70.00x}{(x+0.41)}$	$y=\frac{42.25x}{(x+0.33)}$	$y=\frac{49.10x}{(x+0.39)}$	0.81	0.62	0.60
	Exponential	$y=60.56(1-e^{-2.07x})$	$y=33.81(1-e^{-2.97x})$	$y=38.17(1-e^{-2.66x})$	0.81	0.61	0.60

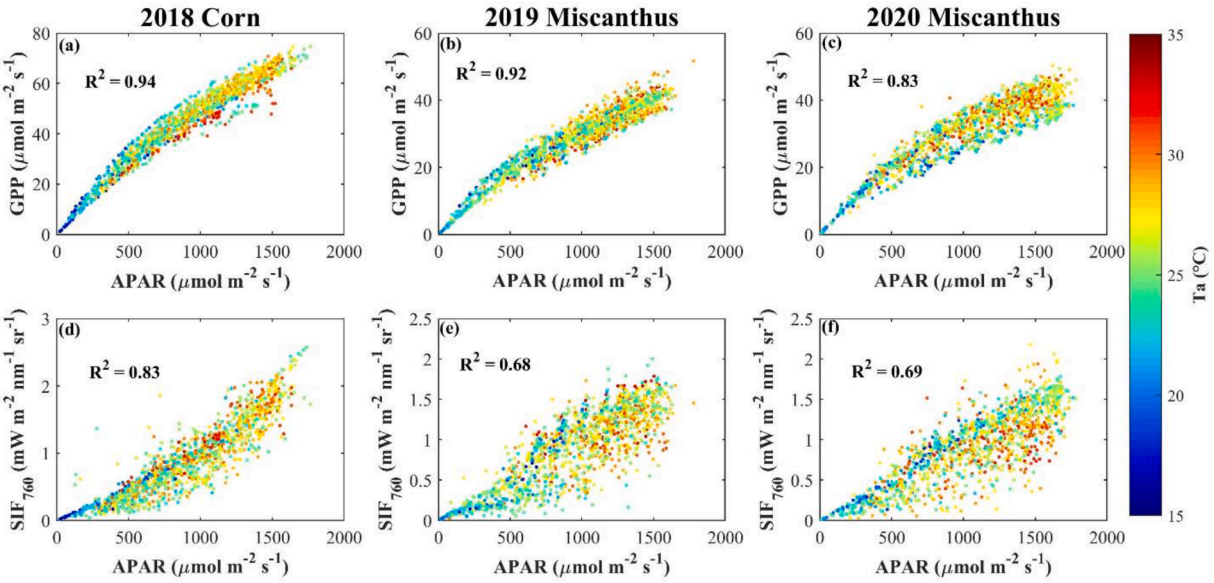

Fig. 4. Relationships of half-hourly GPP and APAR, and of SIF_{760} and APAR over the air temperature (Ta) in (a and d) 2018 corn, (b and e) 2019 miscanthus and (c and f) 2020 miscanthus, respectively. Colormap represented half-hourly Ta. R^2 of the linear regression between SIF_{760} or GPP and APAR were shown in each subfigure. All R^2 values were statistically significant. (For interpretation of the references to color in this figure legend, the reader is referred to the web version of this article.).

in 2018 (GPP: 44.51 μmol m^{-2} s^{-1}; SIF_{760}: 0.92 mW m^{-2} nm^{-1} sr^{-1}) than for miscanthus in 2019 (GPP: 28.31 μmol m^{-2} s^{-1}; SIF_{760}: 0.90 mW m^{-2} nm^{-1} sr^{-1}) and 2020 (GPP: 30.37 μmol m^{-2} s^{-1}; SIF_{760}: 0.78 mW m^{-2} nm^{-1} sr^{-1}). Corn and miscanthus showed different patterns of FPAR, GPP and SIF_{760} from July to August due to their different phenology. For corn, FPAR, GPP and SIF_{760} reached the maximum in early July and maintained the peak until the middle of August, but started to decrease gradually afterwards. For miscanthus, SIF_{760} and GPP were relatively stable from July to August in both years, although FPAR showed an increasing pattern in early July. Peak FPAR was higher in miscanthus (2019: 0.92; 2020: 0.93) compared to corn (2018: 0.89).

3.2. Seasonal relationship between canopy SIF_{760} and GPP in corn and miscanthus

Canopy SIF_{760}- GPP relationship was stronger in corn than in miscanthus at both half-hourly and daily scales for linear, hyperbolic and exponential regressions (Fig. 3 and Table 1). At half-hourly scale, R^2 of

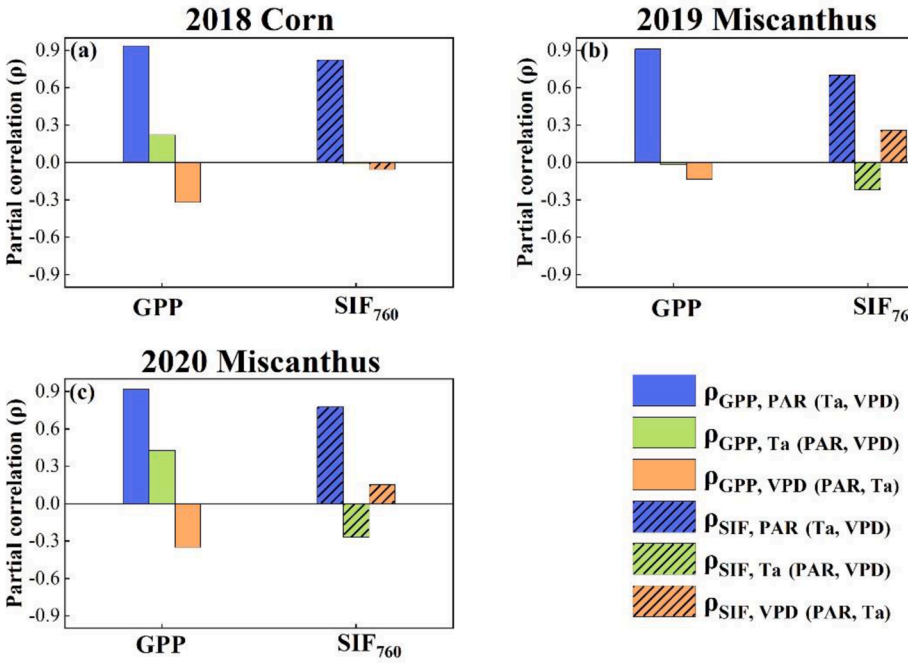

Fig. 5. Partial correlation (ρ) between GPP and environmental variables (solid bars), between SIF_{760} and environmental variables (bars filled with slashes) at half-hourly scale in (a) 2018 corn, (b) 2019 miscanthus and (c) 2020 miscanthus, respectively. Environmental variables included PAR, air temperature (Ta), vapor pressure deficit (VPD). ρ between GPP (or SIF_{760}) and each environmental variable was computed by controlling the other two environmental variables. (For interpretation of the references to color in this figure legend, the reader is referred to the web version of this article.).

linear regression with intercept of SIF_{760}-GPP was 0.77 in 2018 corn, while it was 0.57 and 0.53 in 2019 and 2020 miscanthus, respectively. Hyperbolic and exponential regression improved the SIF_{760}-GPP relationships in 2018 corn (R^2=0.83 and 0.82), 2019 miscanthus (R^2=0.61 and 0.59), and in 2020 miscanthus (R^2=0.57 and 0.56). The R^2 difference between corn and miscanthus were larger on sunny days compared to cloudy days (Table 2). For hyperbolic regression, the R^2 difference between 2018 corn and 2019 miscanthus were 0.39 and 0.17 on sunny days and cloudy days, respectively. Although linear regression with zero intercept of SIF_{760}-GPP showed the highest R^2 among all regressions (Table 1), its root mean square error (RMSE) was substantially larger compared to other regressions (Tables S1 and S2). At daily scale, the R^2 among three regressions were similar for both 2018 corn and 2019 miscanthus. In 2020 miscanthus, hyperbolic and exponential regressions increased R^2 by 0.13 and 0.15, respectively, compared to that of linear regression. Miscanthus daily SIF_{760} showed weak correlation with GPP on sunny days due to the lack of daily variations from July to August in both 2019 and 2020 (Fig. 3).

Linear, hyperbolic and exponential regression models showed significantly different SIF_{760}-GPP relationships between corn and miscanthus at both half-hourly and daily scales (Tables 1 and 2). For half-hourly linear regressions, both fitted slope and intercept were significantly higher in 2018 corn (slope=25.31; intercept=21.09) compared to 2019 (slope=16.02; intercept=13.93) and 2020 miscanthus (slope=15.99; intercept=15.75). No significant difference of the SIF_{760}-GPP relationship between 2019 miscanthus and 2020 miscanthus was observed. R^2 of the hyperbolic regression of SIF_{760}-GPP for corn and miscanthus combined was 0.48 and 0.35 at half-hourly and daily scale, respectively, both of which were lower than the R^2 of miscanthus only and corn only, while RMSE showed the opposite pattern (Fig. S7). This further supported the claim that corn and miscanthus showed different SIF_{760}-GPP relationships. The results from SIF_{760}-GPP_{NT} (Table S3) and from observed raw SIF_{760}-GPP (Table S4) were similar as EC footprint-corrected SIF_{760}-GPP (Table 1), although R^2 of SIF_{760}-GPP_{NT} were overall lower compared to SIF_{760}-GPP.

Both SIF_{760} and GPP showed strong relationships with APAR in corn and miscanthus (Fig. 4). R^2 of the GPP-APAR linear relationship at half-hourly was similar between corn (R^2=0.94) and miscanthus (2019: R^2=0.92; 2020: R^2=0.83), while the APAR-SIF_{760} linear relationship in corn (R^2=0.83) was stronger than that in miscanthus (2019: R^2=0.68; 2020: R^2: 0.69). The GPP_{NT}-APAR relationships were also similar between corn (R^2=0.80) and miscanthus (2019: R^2=0.77; 2020: R^2=0.71 (Fig. S8). This similar GPP-APAR relationship but weaker SIF_{760}-APAR relationship in miscanthus caused the weaker SIF_{760}-GPP relationship compared to corn shown in Fig. 3. For both 2018 corn and 2019 miscanthus, the increasing rate of SIF_{760} with APAR at low APAR conditions was lower compared to that at high APAR conditions while GPP showed a slightly opposite pattern. This resulted in slightly non-linear SIF_{760}-GPP relationships in both species shown in Fig. 3 and Table 1. Both corn and miscanthus GPP tended to increase with Ta. However, corn SIF_{760} showed no response to Ta but miscanthus SIF_{760} tended to decrease with Ta at high APAR conditions.

Partial correlation results further demonstrated the different environmental response of GPP and SIF_{760} in corn and miscanthus (Fig. 5). Both corn and miscanthus GPP showed the strongest positive ρ with PAR, moderate ρ with Ta and moderate negative ρ with VPD, except that in 2019 miscanthus, GPP_{DT} showed no correlation with Ta (Fig. 5b). GPP_{NT} showed similar response to environmental variables as GPP in the three year-sites (Fig. S9). However, the environmental responses of SIF_{760} were different between corn and miscanthus. For 2018 corn, SIF_{760} was mainly controlled by PAR and showed almost no response to Ta and VPD. For 2019 and 2020 miscanthus, SIF_{760} showed a moderate negative ρ with Ta and moderate positive ρ with VPD, which was opposite to GPP. These different responses of GPP and SIF_{760} might contribute to the weaker SIF_{760}-GPP relationship in miscanthus at seasonal scale shown in Fig. 3.

3.3. *Diurnal variations of canopy SIF_{760} and GPP in corn and miscanthus*

Diurnal patterns of sunny-day SIF_{760} and GPP under different Ta and VPD conditions were investigated to further understand the different environmental responses of SIF_{760} and GPP in corn and miscanthus. Normal and high Ta days were separated using daily maximum Ta 30°C as the threshold. A total of 24 normal Ta sunny days and 8 high Ta sunny days were selected in 2018 corn, and 37 normal and 20 high Ta days were selected in combined 2019 and 2020 miscanthus. Similarly, normal and high VPD days were differentiated with daily maximum VPD 20 hPa as the threshold, and 29 normal and 3 high VPD sunny days in

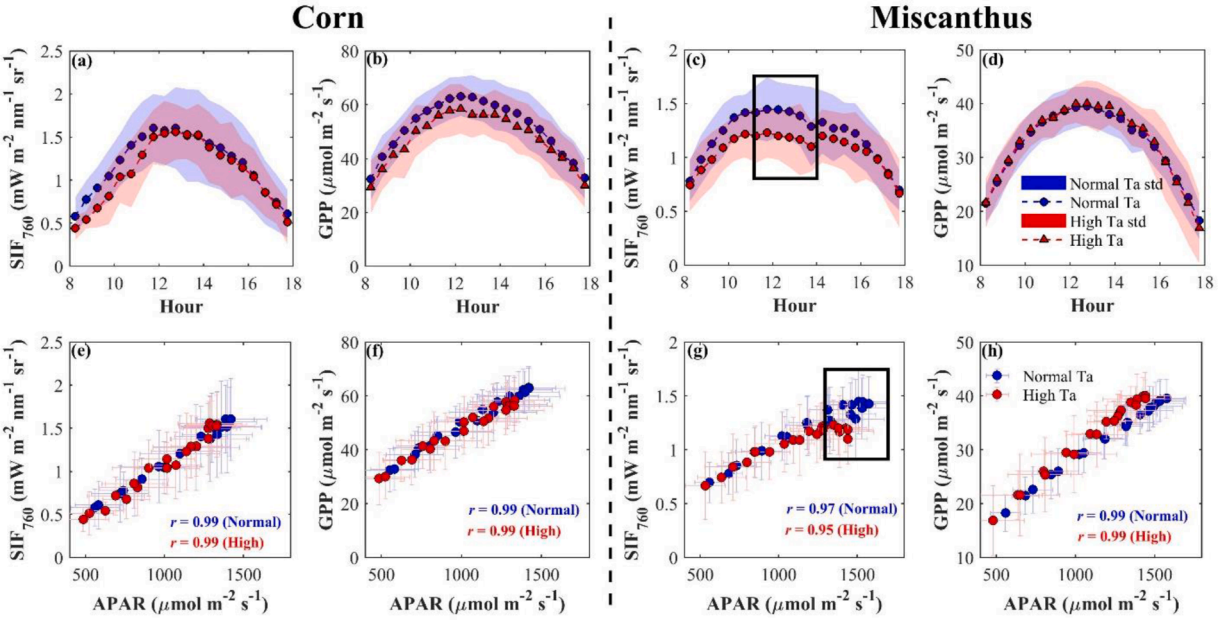

Fig. 6. Diurnal variation of SIF_{760} and GPP under different Ta conditions. The averaged diurnal variation of (a and c) SIF_{760} and (b and d) GPP from normal Ta sunny days (blue) and high Ta sunny days (red) for 2018 corn (left) and combined 2019 and 2020 miscanthus (right). Diurnal relationship (e and g) between APAR and SIF_{760} and (f and h) between APAR and GPP under normal Ta days (blue) and high Ta days (red). Shaded bands in (a–d) represented the standard deviation of averaged SIF_{760} or GPP. Horizontal and vertical error bars in (e–h) indicated the standard deviation of SIF_{760} or GPP and APAR. Black box highlighted the period when SIF_{760} midday depression were observed. The Pearson correlation coefficient (r) between SIF_{760} or GPP and APAR on normal Ta days (blue texts) and high Ta days (red texts) were shown in each subfigure. All r values were statistically significant. (For interpretation of the references to color in this figure legend, the reader is referred to the web version of this article.).

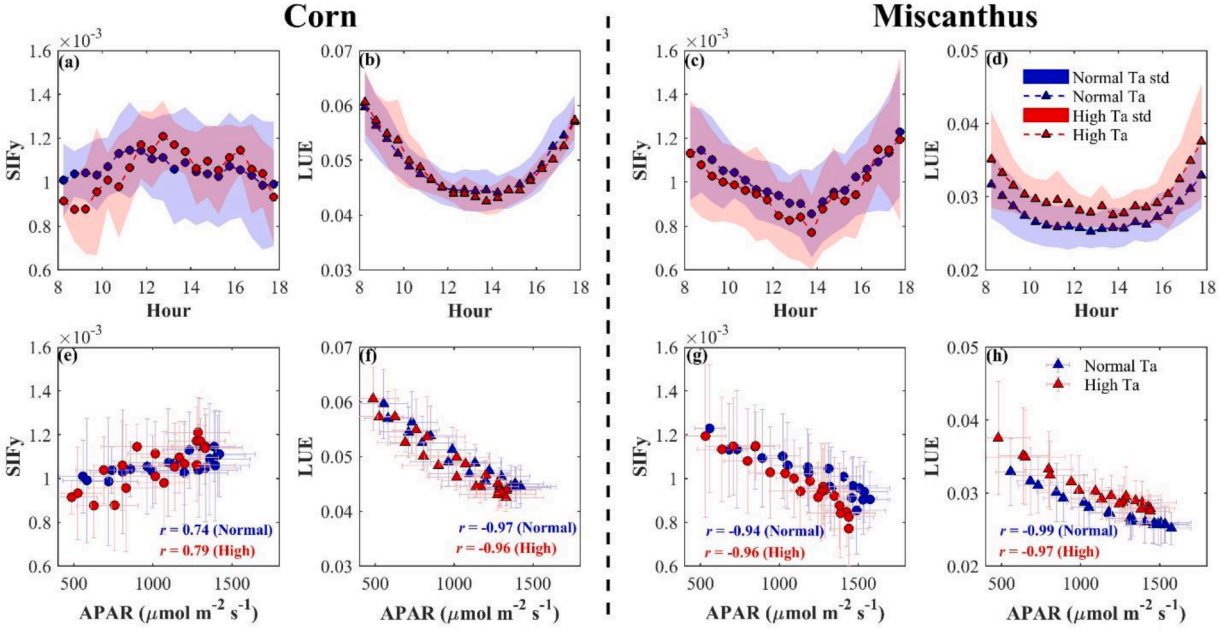

Fig. 7. Diurnal variation of SIFy and LUE under different Ta conditions. The averaged diurnal variation of (a and c) SIFy and (b and d) LUE from normal Ta sunny days (blue) and high Ta sunny days (red) for 2018 corn (left) and combined 2019 and 2020 miscanthus (right). Diurnal relationship (e and g) between APAR and SIFy and (f and h) between APAR and LUE under normal Ta days (blue) and high Ta days (red). Shaded bands in (a–d) represented the standard deviation of averaged SIFy or LUE. Horizontal and vertical error bars in (e–h) indicated the standard deviation of SIFy or LUE and APAR. The Pearson correlation coefficient (r) between SIFy or LUE and APAR on normal Ta and VPD days (blue texts) and high Ta and VPD days (red texts) were shown in each subfigure. All r values were statistically significant. (For interpretation of the references to color in this figure legend, the reader is referred to the web version of this article.).

corn, and 39 normal and 18 high VPD days in miscanthus were found, respectively. Averaged diurnal patterns of SIF_{760} and GPP were obtained for normal and high Ta and VPD days, separately.

Corn and miscanthus showed different diurnal patterns of SIF_{760} and GPP under different Ta and VPD conditions. For corn, SIF_{760} and GPP followed the similar diurnal patterns on both normal and high Ta and VPD days, and both showed a strong linear correlation and similar relationships with APAR under different Ta and VPD conditions (r=0.99,

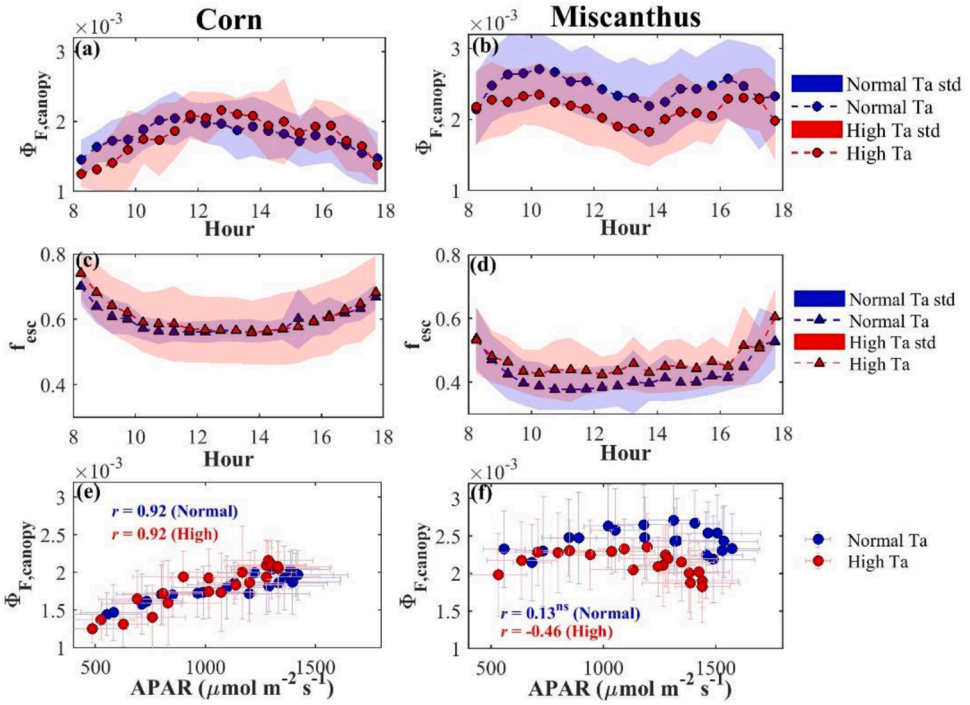

Fig. 8. Diurnal variation of $\Phi_{F,\ Canopy}$ and f_{esc} under different Ta conditions. The averaged diurnal variation of (a and b) $\Phi_{F,\ Canopy}$ and (c and d) f_{esc} from normal Ta sunny days (blue) and high Ta sunny days (red) for 2018 corn (left) and combined 2019 and 2020 miscanthus (right). Diurnal relationship between APAR and under normal Ta days (blue) and high Ta days (red) in (e) corn and (f) miscanthus. Shaded bands in (a–d) represented the standard deviation of averaged $\Phi_{F,\ Canopy}$ or f_{esc}. Horizontal and vertical error bars in (e and f) indicated the standard deviation of $\Phi_{F,\ Canopy}$ and f_{esc} or APAR. The Pearson correlation coefficient (r) between $\Phi_{F,\ Canopy}$ and APAR on normal Ta days (blue texts) and high Ta days (red texts) were shown in each subfigure. "ns" indicated that $\Phi_{F,\ Canopy}$ and APAR were not significantly correlated. Other r values were statistically significant. (For interpretation of the references to color in this figure legend, the reader is referred to the web version of this article.).

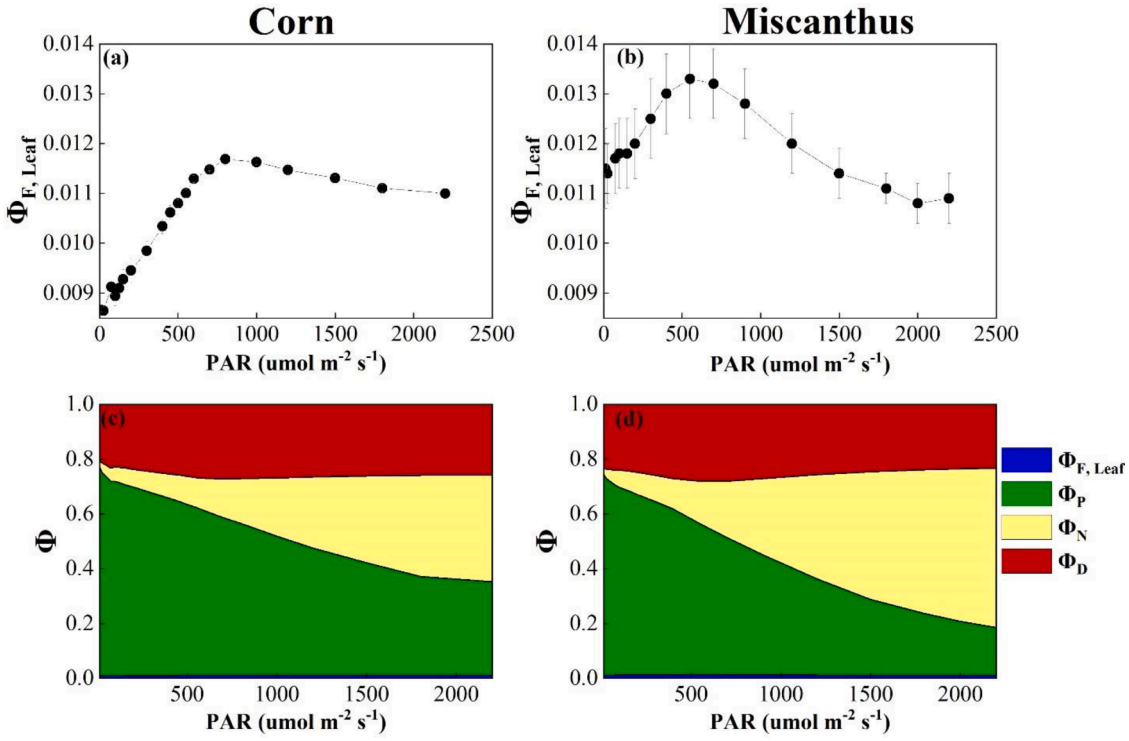

Fig. 9. Energy partitioning of top leaves in 2018 corn (left) and 2019 miscanthus (right) under different PAR levels from the light response curves. Relationship between leaf-level $\Phi_{F,\ Leaf}$ and PAR in (a) corn and (b) miscanthus. Energy partitioning ($\Phi_{F,\ Leaf}$, Φ_P, Φ_N and Φ_D) of top leaves in (c) corn and (d) miscanthus. Measurements were taken at the corn site on DOY 198-199 in 2018 (for corn) and at the Miscanthus site on DOY 187, DOY 194, DOY 209, DOY 215 and DOY 242 in 2019 (for miscanthus). (For interpretation of the references to color in this figure legend, the reader is referred to the web version of this article.).

Figs. 6 and A1). For miscanthus, different behaviors of SIF_{760} and GPP were found. SIF_{760} was overall lower on high Ta days compared to normal Ta days, while GPP showed the opposite pattern (Fig. 6). Miscanthus GPP followed the diurnal pattern of APAR and they were strongly and linearly correlated on both normal and high Ta and VPD days (r=0.99, Figs. 6 and A1). However, miscanthus SIF_{760} showed a flatter daytime variation compared to GPP overall, and even a midday depression under high Ta and VPD days (indicated by the black box in Figs. 6 and A1). SIF_{760} stopped increasing with APAR at high APAR conditions on high Ta and VPD days which resulted in an overall weaker

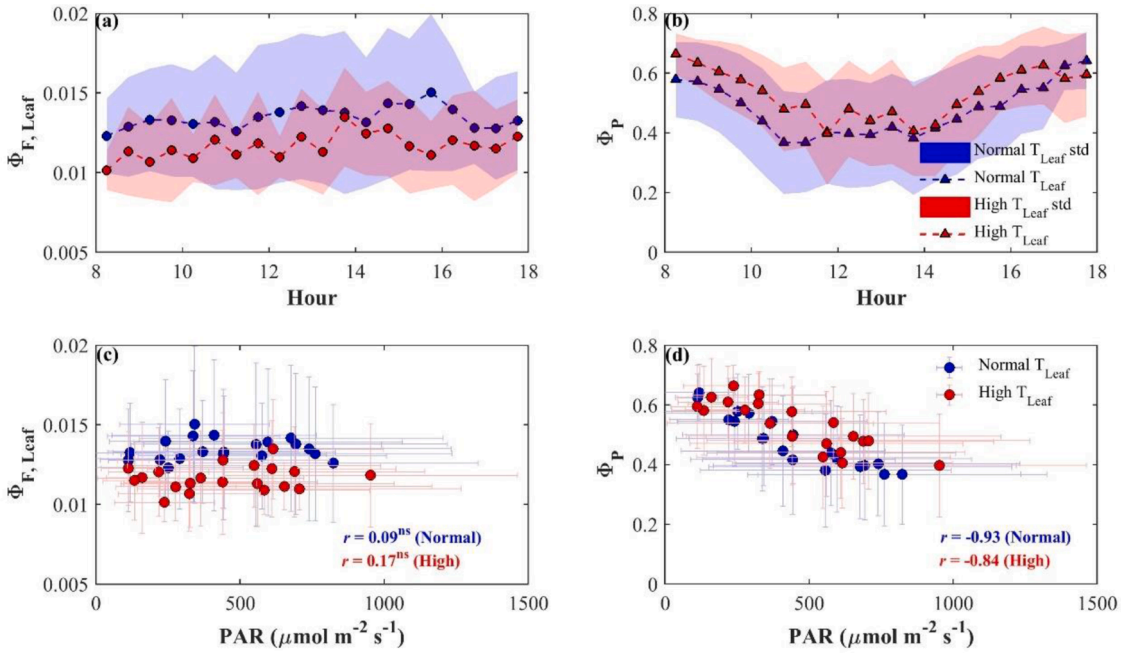

Fig. 10. Diurnal averaged pattern of leaf-level fluorescence yield ($\Phi_{F,\ Leaf}$) and photochemical yield (Φ_P), and their relationships with PAR of top leaves in 2020 miscanthus from the Moni-PAM measurements from July to August. (a) Averaged diurnal pattern of $\Phi_{F,\ Leaf}$ from normal T_{Leaf} days (blue dots) and high T_{Leaf} days (red dots); (b) averaged diurnal pattern of Φ_P from normal T_{Leaf} days (black triangles) and high T_{Leaf} days (red triangles); (c) diurnal relationships between averaged Φ_F and PAR under normal (blue) and high T_{Leaf} days (red); (d) diurnal relationships between averaged Φ_P and PAR under normal (blue) and high T_{Leaf} days (red). Shaded bands in (a and b) represented the standard deviation (std) of averaged $\Phi_{F,\ Leaf}$ or Φ_P. Horizontal and vertical error bars in (c and d) indicated the standard deviation of normalized $\Phi_{F,\ Leaf}$ or Φ and PAR. The Pearson correlation coefficient (r) between normalized $\Phi_{F,\ Leaf}$ or Φ and PAR on normal T_{Leaf} days (blue texts) and high $_{Leaf}$ days (red texts) were shown in each subfigure. "ns" indicated that Φ_F and PAR were not significantly correlated. Other r values were statistically significant. (For interpretation of the references to color in this figure legend, the reader is referred to the web version of this article.).

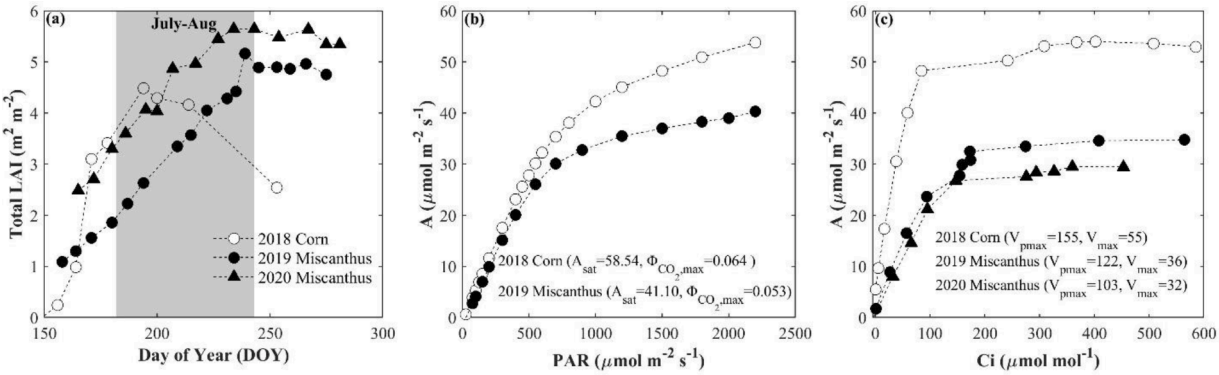

Fig. 11. (a) Seasonal variation of total LAI in 2018 corn (open circles), 2019 miscanthus (filled circles) and 2020 miscanthus (filled triangles) measured by LAI-2200C plant canopy analyzer near the SIF tower; (b) representative responses of leaf assimilation rate (A) to incident PAR in 2018 corn (open circles) and 2019 miscanthus (filled circles); (c) representative responses of leaf assimilation rate (A) to intracellular CO_2 concentration (Ci) of 2018 corn (open circles), 2019 miscanthus (filled circles) and 2020 miscanthus (filled triangles). The shaded area in (a) indicates the period of July to August. The A-PAR and A-Ci curves of corn were measured using LI-6800 on July, 17th of 2018 and the curves of miscanthus were measured on July, 13th of 2019 and July, 13th of 2020. Fitted values of light-saturated leaf photosynthesis (A_{sat}) and maximum quantum yield of CO_2 assimilation ($\Phi_{CO2,max}$) from A-PAR curves, and V_{pmax} and V_{max} from the A-Ci curves were shown in the figure. For all curves, leaf temperature and chamber relative humidity were controlled at 27°C and 55%, respectively.

SIF_{760}-APAR relationship (r=0.91-0.95). The different environmental responses of SIF_{760} and GPP in miscanthus caused an overall weaker diurnal correlation of SIF_{760}-GPP (r=0.78±0.16) compared to corn (r=0.90±0.08) (Fig. S10).

3.4. Environmental responses of canopy SIFy and LUE

Corn and miscanthus SIFy and LUE showed different responses to environmental conditions. Overall, miscanthus LUE was lower than corn LUE while SIFy was similar between the two species. Corn SIFy and LUE did not show considerably different responses to Ta, but miscanthus SIFy and LUE showed the opposite responses to Ta with overall lower SIFy but higher LUE observed on high Ta days (Fig. 7). Corn SIFy was characterized by an overall bell shape, i.e., slightly higher at noon than morning and afternoon on both normal and high Ta and VPD days, and it showed overall positive correlation with APAR (Figs. 7 and A2). Miscanthus SIFy showed completely different diurnal patterns than corn. Miscanthus SIFy was characterized by a bowl shape, with the minimum value appearing at noon, and miscanthus SIFy and APAR was negative correlated on both normal and high Ta and VPD days. Larger decrease of

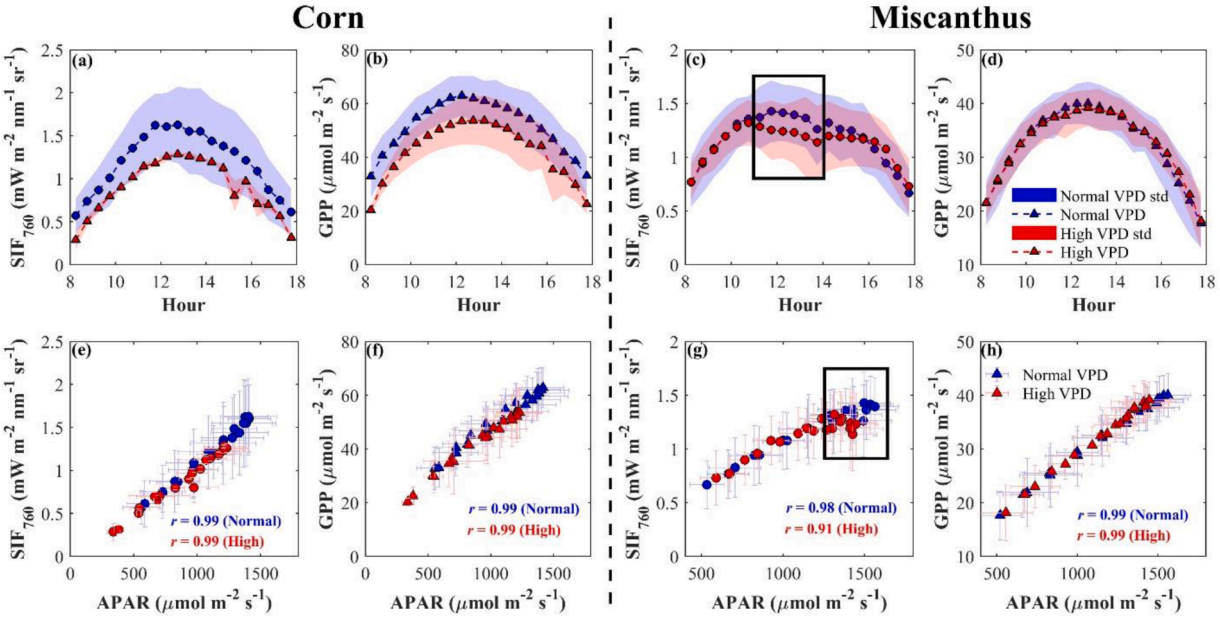

Fig. A1. Diurnal variation of SIF_{760} and GPP under different VPD conditions. The averaged diurnal variation of (a and c) SIF_{760} and (b and d) GPP from normal VPD sunny days (blue) and high VPD sunny days (red) for 2018 corn (left) and combined 2019 and 2020 miscanthus (right). Diurnal relationship (e and g) between APAR and SIF_{760} and (f and h) between APAR and GPP under normal VPD days (blue) and high VPD days (red). Shaded bands in (a–d) represented the standard deviation of averaged SIF_{760} or GPP. Horizontal and vertical error bars in (e–h) indicated the standard deviation of SIF_{760} or GPP and APAR. Black box highlighted the period when SIF_{760} midday depression were observed. The Pearson correlation coefficient (r) between SIF_{760} or GPP and APAR on normal VPD days (blue texts) and high VPD days (red texts) were shown in each subfigure. All r values were statistically significant. Daytime maximum VPD ranged from 12hPa to 20hPa on normal days and from 20hPa to 25hPa for high VPD days, respectively. (For interpretation of the references to color in this figure legend, the reader is referred to the web version of this article.).

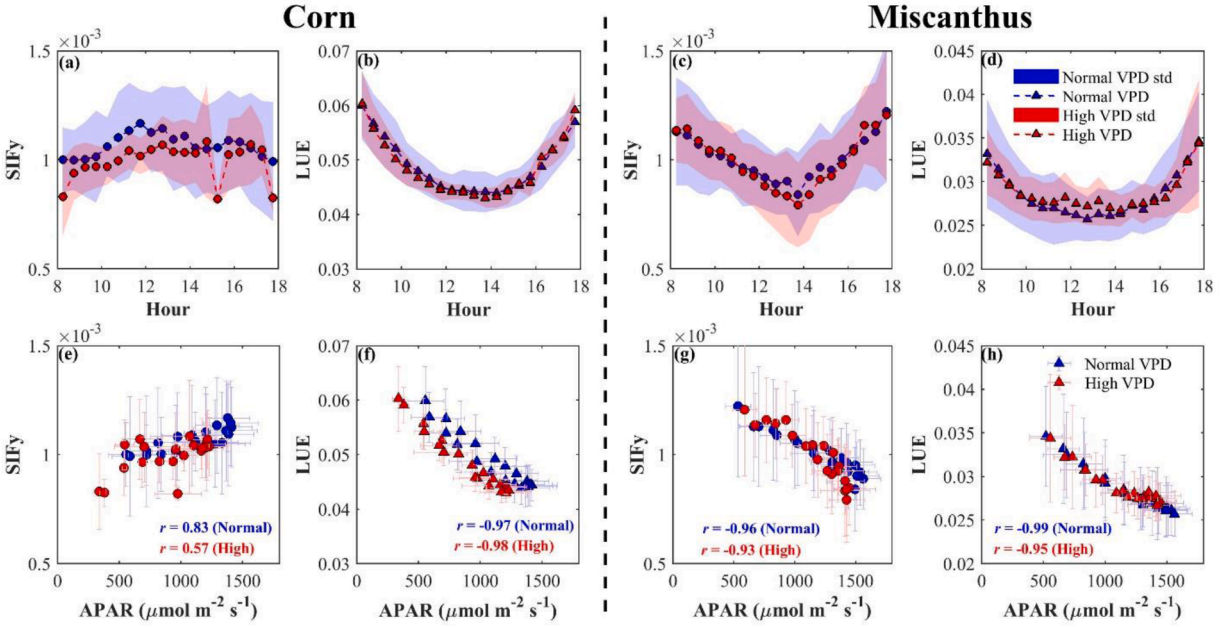

Fig. A2. Diurnal variation of SIFy and LUE under different Ta conditions. The averaged diurnal variation of (a and c) SIFy and (b and d) LUE from normal Ta sunny days (blue) and high Ta sunny days (red) for 2018 corn (left) and combined 2019 and 2020 miscanthus (right). Diurnal relationship (e and g) between APAR and SIFy and (f and h) between APAR and LUE under normal Ta days (blue) and high Ta days (red). Shaded bands in (a–d) represented the standard deviation of averaged SIFy or LUE. Horizontal and vertical error bars in (e–h) indicated the standard deviation of SIFy or LUE and APAR. The Pearson correlation coefficient (r) between SIFy or LUE and APAR on normal Ta and VPD days (blue texts) and high Ta and VPD days (red texts) were shown in each subfigure. All r values were statistically significant. (For interpretation of the references to color in this figure legend, the reader is referred to the web version of this article.).

SIFy with APAR was observed at high APAR, VPD and Ta conditions compared to low APAR, Ta and VPD conditions (Figs. 7 and A2). For the diurnal variation of LUE, both species showed an overall bowl shape of diurnal LUE with minimum values at noon, and strong negative LUE-APAR correlations (Figs. 7 and A2).

Diurnal patterns of $\Phi_{F,\ Canopy}$ and f_{esc} were further investigated to

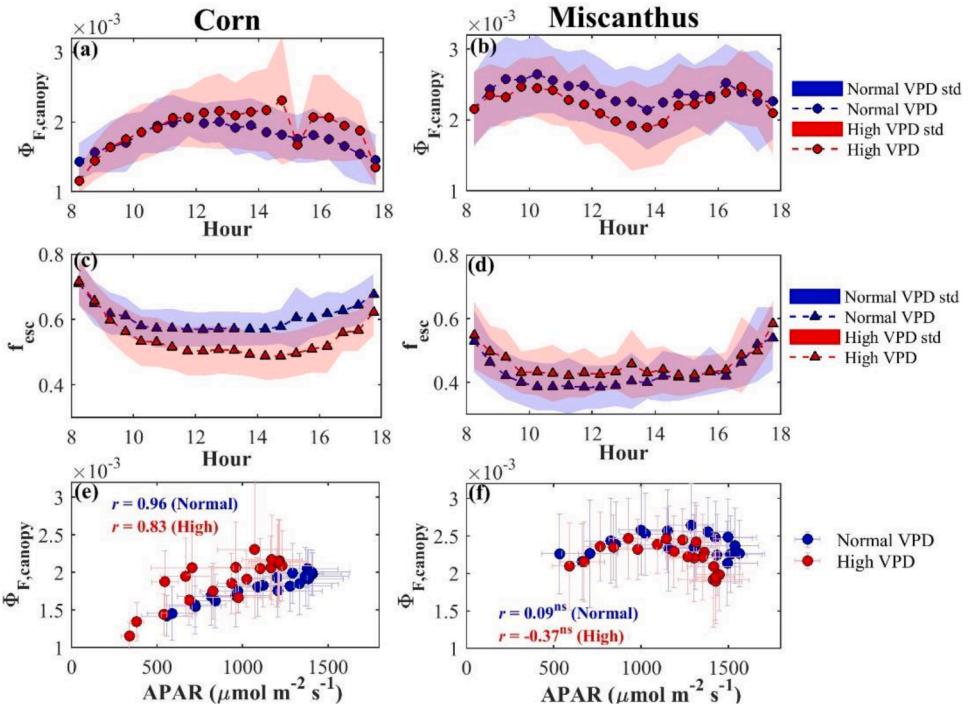

Fig. A3. Diurnal variation of $\Phi_{F,\ Canopy}$ and f_{esc} under different VPD conditions. The averaged diurnal variation of (a and b) $\Phi_{F,\ Canopy}$ and (c and d) f_{esc} from normal VPD sunny days (blue) and high VPD sunny days (red) for 2018 corn (left) and combined 2019 and 2020 miscanthus (right). Diurnal relationship between APAR and under normal VPD days (blue) and high VPD days (red) in (e) corn and (f) miscanthus. Shaded bands in (a–d) represented the standard deviation of averaged $\Phi_{F,\ Canopy}$ or f_{esc}. Horizontal and vertical error bars in (e and f) indicated the standard deviation of $\Phi_{F,\ Canopy}$ and f_{esc} or APAR. The Pearson correlation coefficient (r) between $\Phi_{F,\ Canopy}$ and APAR on normal VPD days (blue texts) and high Ta days (red texts) were shown in each subfigure. "ns" indicated that $\Phi_{F,\ Canopy}$ and APAR were not significantly correlated. Other r values were statistically significant. (For interpretation of the references to color in this figure legend, the reader is referred to the web version of this article.).

understand the different behaviors of SIFy in corn and miscanthus, and different behaviors of $\Phi_{F,\ Canopy}$ were observed between the two species. Overall, miscanthus $\Phi_{F,\ Canopy}$ was higher than corn due to its lower f_{esc} compared to corn (Fig. 8). Similar as corn SIFy, corn $\Phi_{F,\ Canopy}$ was characterized by a bell shape with maximum at noon time, and it showed strong positive correlation with APAR (r=0.83-0.96, Figs. 8 and A3). However, miscanthus $\Phi_{F,\ Canopy}$ was characterized by an M shape, i.e., $\Phi_{F,\ Canopy}$ first increased in the morning, then decreased at noon, and then increased again in the afternoon. Miscanthus $\Phi_{F,\ Canopy}$ first increased with APAR at low light to medium conditions and decreased with APAR under high light conditions (Figs. 8and A3). This decrease was even larger on high Ta and VPD days, resulting in an overall negative $\Phi_{F,\ Canopy}$-APAR correlation on high Ta (r=-0.46) and high VPD days (r=-0.37). Both corn and miscanthus f_{esc} showed a bowl-shape diurnal pattern, with large values in the early morning and late afternoon but stable and small values in the midday (Figs. 8 and A3). This diurnal pattern of f_{esc} amplified the diurnal variation of miscanthus SIFy shown in Fig. 7.

3.5. Environmental responses of leaf quantum yields

Leaf-level $\Phi_{F,\ Leaf}$ showed different responses to PAR between corn and miscanthus. Consistent with canopy-level results, miscanthus showed overall higher $\Phi_{F,\ Leaf}$ than corn. Corn $\Phi_{F,\ Leaf}$ first increased with PAR and slightly decreased with PAR when PAR was higher than ~800 μmol m^{-2} s^{-1} (Fig. 9a), with an overall increase trend with PAR (r=0.72). Miscanthus $\Phi_{F,\ Leaf}$ first increased with PAR and then strongly decreased with the PAR increase beyond ~550 μmol m^{-2} s^{-1} (Fig. 9b). Leaf-level Φ_P overall showed a decreasing trend with PAR increasing for both species. However, the decreasing rate of miscanthus Φ_P was larger than that of corn, resulting in a lower miscanthus Φ_P under the same high PAR conditions (Fig. 9c and d). Φ_N increased with PAR for both species, but with a higher increasing rate shown in miscanthus, which resulted in a high Φ_N in miscanthus compared to corn under the same light. Φ_D remained relatively stable with PAR changes for both species.

Averaged diurnal patterns of leaf-level $\Phi_{F,\ Leaf}$, Φ_P and Φ_N under normal and high T_{leaf} days were obtained for miscanthus from the Moni-PAM dataset to be comparable with the canopy-level results. Normal and high T_{Leaf} days were defined as days when daily maximum T_{Leaf} was lower and higher than 38°C, respectively. A higher threshold was chosen for T_{leaf} than for Ta because of generally higher T_{leaf} than Ta (Fig. S11). Consistent with canopy-level results, miscanthus $\Phi_{F,\ Leaf}$ was overall lower on high T_{Leaf} days while Φ_P was slightly higher on high T_{leaf} days compared to normal days (Fig. 10a). $\Phi_{F,\ Leaf}$ showed less diurnal variations compared to canopy-level $\Phi_{F,\ Canopy}$, but a weak trend that $\Phi_{F,\ Leaf}$ first increased with PAR and then decreased with PAR on both normal and high T_{Leaf} days was observed (Fig. 10c). With the exclusion of data under low light (PAR<400 μmol m^{-2} s^{-1}), r of $\Phi_{F,\ Leaf}$-PAR were -0.34 and -0.21 on normal and high T_{Leaf} days, respectively. Averaged miscanthus leaf Φ_P showed a bowl-shaped diurnal pattern with minimum values at noon (Fig. 10b). Φ_P and PAR were strongly negatively correlated on both normal (r=-0.93) and high T_{Leaf} days (r=-0.84) (Fig. 10d).

4. Discussion

We explored the canopy SIF_{760}-GPP relationships in two C4 crops, corn and miscanthus using continuous in situ canopy measurements. We found that the SIF_{760}-GPP relationship was different between corn and miscanthus with higher R^2 and slope of SIF_{760}-GPP shown in corn compared to miscanthus. Here we first provide a detailed discussion about the different SIF_{760}-GPP relationships observed the two species in terms of R^2 from both the roles of leaf-level energy partitioning and canopy structure perspectives, and then discuss the different slopes of SIF_{760}-GPP in corn and miscanthus as well as the implications for SIF-based GPP estimation.

4.1. Leaf-level absorbed energy partitioning in corn and miscanthus

Different leaf-level energy partitioning among photochemistry, fluorescence and heat dissipation under varying environmental conditions plays an important role in the observed different SIF_{760} patterns between corn and miscanthus. Under low light conditions (e.g. PAR < 500 μmol m^{-2} s^{-1}), Φ_P dominates the energy partitioning of APAR, and both $\Phi_{F,\ Leaf}$ and Φ_N are low (Baker, 2008). Under high light conditions (e.g. PAR > 500 μmol m^{-2} s^{-1}), Φ_N increases (Müller et al., 2001), and both Φ_P and $\Phi_{F,\ Leaf}$ decrease (Porcar-Castell et al., 2014). For

miscanthus, Φ_N strongly increased with PAR, causing an even lower $\Phi_{F,\ Leaf}$ under high light conditions compared to that under low light conditions. For corn, the Φ_N increase with PAR decelerated under high light conditions, resulting in a relatively small decrease of $\Phi_{F,\ Leaf}$ and an overall higher $\Phi_{F,\ Leaf}$ under high PAR compared to low PAR. These different responses of $\Phi_{F,\ Leaf}$ to light led to the different diurnal canopy $\Phi_{F,\ Canopy}$ patterns between corn and miscanthus (Fig. 8). Ta and VPD further affect the energy partitioning (Peguero-Pina et al., 2008; Van Der Tol et al., 2014; Chou et al., 2017). Previous studies have found that $\Phi_{F,\ Leaf}$ decrease under high temperature and VPD with the increasing of Φ_N (Flexas et al., 2002; Peguero-Pina et al., 2008; Ač et al., 2015). Miscanthus tends to show a stronger response to Ta and VPD, with a stronger decline of Φ_F and a stronger increase of Φ_N compared to corn under high Ta and VPD conditions. Additionally, such decline of Φ_F under high light conditions tends to be larger compared to low light conditions for both species (Van Der Tol et al., 2014). The overall lower $\Phi_{F,\ Leaf}$, Φ_N, $\Phi_{F,\ Canopy}$ in corn indicates that corn tends use more APAR for photochemistry and less APAR for fluorescence and heat dissipation and the energy partitioning of APAR is less sensitive to Ta and VPD, while miscanthus tends to strongly reduce fluorescence emission to maintain photochemistry under high PAR, Ta and VPD conditions. Different maximum carboxylation rates (V_{max}) may contribute to the different responses of $\Phi_{F,\ Leaf}$ ($\Phi_{F,\ Canopy}$) to environmental conditions in corn and miscanthus. Corn tends to have higher V_{max} than miscanthus (Fig. 11, corn Vmax=55 umol m^{-2} s^{-1}; miscanthus Vmax=32-36 umol m^{-2} s^{-1}) (Dohleman and Long, 2009), which leads to less $\Phi_{F,\ Leaf}$ decline compared to miscanthus under the same high light conditions (Frankenberg and Berry, 2018).

4.2. The role of canopy structure in the observed SIF_{760} pattern

Canopy structure contributes to the larger diurnal variation in canopy level $\Phi_{F,\ Canopy}$ compared to leaf level $\Phi_{F,\ Leaf}$ shown in miscanthus as well as different diurnal canopy $\Phi_{F,\ Canopy}$ and SIFy patterns (Figs. 7, 8 and 10). $\Phi_{F,\ Canopy}$ depends on both leaf-level $\Phi_{F,\ Leaf}$ and the relative contribution of sunlit and shaded leaves (Yang et al., 2021). Shaded leaves experience lower incident PAR and less variation of PAR across the day (Jifon and Syvertsen, 2003; Retkute et al., 2018). For both species, sunlit leaves contribute more than 70% of canopy total carbon assimilation (Dohleman and Long, 2009). Therefore, the diurnal variation of canopy $\Phi_{F,\ Canopy}$ is mainly determined by the diurnal variation of sunlit leaves fraction which generally follows a bell-shaped pattern with the highest value at noon (De Pury and Farquhar, 1997) and the variation of sunlit leaves incident PAR. For corn, the high sunlit leaf fraction combined with high sunlit leaf $\Phi_{F,\ Leaf}$ caused a higher canopy $\Phi_{F,\ Canopy}$ at noon than early morning and late afternoon. By contrast, for miscanthus, the low sunlit leaf Φ_F combined with high sunlit leaf fraction resulted in a larger decrease of miscanthus canopy $\Phi_{F,\ Canopy}$ than the leaf $\Phi_{F,\ Leaf}$ at noon to afternoon time. Additionally, the role of f_{esc} complicated the observed SIF_{760} pattern. With low solar zenith angle in early morning and late afternoon, f_{esc} calculated by directional NIRv is larger than the f_{esc} at the midday (Zeng et al., 2019). For corn, the high $\Phi_{F,\ Canopy}$ at noon time decreased for SIFy, resulting in a weaker positive SIFy-APAR correlation compared to $\Phi_{F,\ Canopy}$-PAR. For miscanthus, the higher $\Phi_{F,\ Canopy}$ in the morning and afternoon and lower $\Phi_{F,\ Canopy}$ at noon time was amplified for SIFy, which caused a strong negative SIFy-APAR correlation. The strong decline of miscanthus SIFy under high PAR, high Ta and VPD conditions resulted in the midday-afternoon SIF_{760} reduction, causing SIF_{760} to deviate from APAR at diurnal scale and weakening the diurnal SIF_{760}-GPP relationships. However, f_{esc}-corrected total SIF emitted by all leaves (SIF_{total}) still showed a SIF_{760} midday depression in miscanthus (Fig. S12), indicating that large decline of $\Phi_{F,\ Canopy}$ at high PAR conditions might be the major reason for the observed SIF_{760} midday depression in miscanthus, although the current f_{esc} estimation still exists uncertainty (Zeng et al., 2019). The observed different SIF_{760} behaviors as well as different SIF_{760}-GPP relationships between corn and miscanthus in our study are resulted from the combined effect of their different leaf-level absorbed energy partitioning, and canopy structure including the change of sunlit leaf fraction. It is worth mentioning that SIF midday depression under high PAR and VPD conditions has been reported in forest and winter barley (Paul-Limoges et al., 2018; Gu et al., 2019b). Although a recent study has found SIF midday depression in corn, it was due to the midday depression of APAR caused by the row structure impact (Chang et al., 2021), which is not contrast to our corn results since no APAR midday depression was shown in our corn dataset.

4.3. Different slopes of SIF_{760}-GPP in corn and miscanthus

A higher slope of SIF_{760}-GPP in corn compared to miscanthus was found, due to a larger difference in GPP magnitude than SIF_{760} magnitude between corn and miscanthus. Higher corn GPP than miscanthus during mid-summer have been shown in previous studies (Moore et al., 2021), which is due to higher corn leaf assimilation rate (A) during peak growing season (Dohleman and Long, 2009). The higher A in corn compared to miscanthus is due to less biochemical limitations indicated by higher V_{max}, higher maximum phosphoenolpyruvate (PEP) regeneration rate (V_{pmax}), higher light-saturated leaf photosynthesis (A_{sat}) and higher $\Phi_{CO2,max}$ in corn compared to miscanthus (Dohleman and Long, 2009) (Fig. 11). Model simulations have shown that higher V_{max} could lead to higher slope of SIF_{760}-GPP since GPP is more sensitive to V_{max} compared to SIF_{760} (Zhang et al., 2016; Hao et al., 2021). LAI and leaf angle distribution (LAD) are also important for the SIF_{760}-GPP relationship (Hao et al., 2021). From July to August, miscanthus total LAI continued to increase while corn LAI reached the maximum around middle of July. The mean LAI from July to August of corn was higher than 2019 miscanthus but lower than 2020 miscanthus. However, the slope of SIF_{760}-GPP in both 2019 and 2020 miscanthus was lower than that in 2018 corn, indicating that LAI is not the major reason causing the different slopes between corn and miscanthus. The lower impact of LAI on slopes of SIF_{760}-GPP might be related to that both cropping systems reached LAI values of LAI (around 4 m^2 m^{-2}) where the slope of SIF_{760}-GPP has been shown to be insensitive to further increases in LAI (Zhang et al., 2016; Zhou et al., 2020). Miscanthus LAD was close to spherical distribution and remained relatively stable from July to August from the manual leaf angle measurements (Fig. S13). No direct LAD measurements were made in corn in this study, but no substantial LAD difference between corn and miscanthus are expected since the a previous study at the same sites has showed that contribution from sunlit leaves to total canopy photosynthesis is similar between the two species (Dohleman and Long, 2009). Therefore, higher leaf photosynthesis during peak growing season is expected to be the main reason for the higher slopes of SIF_{760}-GPP in corn compared to miscanthus.

4.4. Sources of uncertainties in this study

We acknowledge that there are three main uncertainties in this study including the footprint correction of nadir-view SIF_{760}, NEE partitioning for GPP estimation uncertainty, and the limited leaf-level measurements. Footprint correction of SIF_{760} was used to adjust the spatial mismatch between SIF_{760} and GPP observations, which aimed to reduce the uncertainty of comparing SIF_{760}-GPP relationships in corn and miscanthus. We note that the method we used to correct nadir SIF_{760} to EC footprint-based SIF has uncertainties since we did not consider the variation of PAR between the SIF pixel and the EC footprint, and the variation of SIF-NIRvP relationships. No PAR variation within radius 500 m in the field is valid during sunny conditions (Jiang et al., 2020), although this assumption might bring some uncertainties under scattered cloudy conditions. Regarding the variation of SIF-NIRvP relationships, recent cross-scale studies have found that NIRvP can explain around 80% of SIF variations when combing spatial and temporal scales (Kimm et al., 2021; Dechant et al., 2022), indicating that our method

can capture the majority of SIF difference between EC footprint and SIF tower area. Additionally, the stronger SIF_{760}-GPP and higher slope of SIF_{760}-GPP in corn still held when using raw nadir-view SIF_{760} observations (Table S4), which further confirmed the different SIF_{760}-GPP relationships between the two species.

We are aware of that GPP was not directed measured but estimated from EC NEE. Different partitioning methods may bring some uncertainties into GPP estimation and further SIF_{760}-GPP relationships. In this study, we tried both standard nighttime method (GPP_{NT}) and daytime method (GPP_{DT}). Generally, GPP_{DT} showed a stronger relationship with SIF_{760} compared to nighttime method since radiation was used to model GPP in GPP_{DT} (Lasslop et al., 2010), and GPP_{NT} showed slightly higher magnitude compared to GPP_{DT} possibly due to the overestimation of daytime ER by directly extrapolating nighttime ER model to daytime (Keenan et al., 2019). However, these slight differences between the two NEE partitioning methods do not influence the comparison between corn and miscanthus, which is the major focus of this study. Other NEE partitioning methods are emerging recently, and their uncertainties may need further explored. Isotope measurements may overcome the overestimation of daytime ER and yield reasonable light use efficiency response to environment (Wehr et al., 2016). Recent studies have utilized SIF for NEE partitioning (Kira et al., 2021; Zhan et al., 2022), but the scalability of this method still needs more test. More studies are needed to understand how different NEE partitioning methods perform in different ecosystems under various environmental conditions. More robust and direct in situ GPP estimation such as carbonyl sulfide (Kooijmans et al., 2019; Stinecipher et al., 2022) is needed to accurately quantify regional and global GPP.

We also note that limited leaf-level gas exchange and PAM measurements in corn were used to explain the different SIF_{760} behaviors between corn and miscanthus. In this study, we only focused on July and August when canopies were fully closed and were photosynthetically active. Miscanthus $\Phi_{F,\ Leaf}$-PAR relationships conducted from five dates from July-August in 2019 showed the consistent pattern, with the first increase of $\Phi_{F,\ Leaf}$ with PAR and then decrease of $\Phi_{F,\ Leaf}$ when PAR was higher than 550 μmol m^{-2} s^{-1} (Fig. S14). This indicates that although leaf-level measurements in corn was only conducted in the middle of July, no substantial change of leaf-level results is expected from July to August. Therefore, we justify that these uncertainties do not affect our general conclusions.

4.5. Implications for GPP estimations

The considerably different SIF_{760}-GPP relationships (both in R^2 and slope) between the two C4 crops, annual corn and perennial miscanthus, demonstrate that SIF-GPP relationships vary within the same PFT. Establishing one SIF-GPP relationship for one PFT to estimate GPP would increase the uncertainty of GPP estimation (Zhang et al., 2020a). Different species within the same PFT still show differences in canopy structure and leaf physiology (e.g., corn vs miscanthus in this study). Porcar-Castell et al. (2021) have summarized the importance of instrumentation, algorithms, canopy structure and leaf physiology in affecting the decouples/couples of SIF and GPP. In this study, we used the same protocol for instrument setup, data collection and data processing for side-by-side corn and miscanthus, which eliminated the uncertainty caused by climate, instrumentation and algorithms. Many studies have discussed the importance of canopy structure in determining the SIF-GPP relationships in crops (Miao et al., 2018; Dechant et al., 2020). Our study further demonstrated the importance of leaf physiology, both energy partitioning in the light reactions of photosynthesis and biochemical limitations in the dark reactions of photosynthesis, in determining the SIF-GPP relationships. Leaf-level PAM measurements and leaf physiology parameters such as V_{max} in tandem with canopy level observations are essential to better understand the SIF-GPP relationships. Most previous studies focus on a single crop, and the comparison between different studies is complicated by different instrumentations (Yang et al., 2018a, 2021; He et al., 2020). More in situ canopy and leaf-level observations that cover more species and environmental conditions with the same instrument and data protocol would be helpful to better understand the SIF-GPP relationships.

5. Conclusions

We investigated the canopy SIF_{760} and GPP relationships in two C4 crops, corn and miscanthus, using continuous in situ measurements for both species. We found considerably different SIF_{760}-GPP relationships between corn and miscanthus. First, canopy SIF_{760} in corn was found to explain more variations (~80%) in GPP compared to that in miscanthus (~60%) at half-hourly scale. This difference was mainly caused by different leaf-level energy partitioning of fluorescence, photochemistry and heat dissipation between corn and miscanthus. For miscanthus, high NPQ under high PAR, Ta and VPD conditions caused a large decline of $\Phi_{F,\ Leaf}$ and $\Phi_{F,\ Canopy}$, and further led to a SIF_{760} midday depression and deviation SIF_{760} from APAR, which weakened the SIF_{760}-GPP relationship. For corn, $\Phi_{F,\ Leaf}$ showed a relatively small response to environmental change compared to miscanthus, and both GPP and SIF_{760} were dominated by APAR. Second, the slopes of corn SIF_{760}-GPP at half-hourly scale were higher than that in miscanthus due to higher GPP magnitude in corn but relatively similar SIF_{760} magnitudes in corn and miscanthus. Higher GPP in corn was largely attributed to the higher leaf-level photosynthesis during middle summer caused by less biochemical limitations (e.g. higher carboxylate rate, higher phosphoenolpyruvate regeneration rate and higher maximum quantum efficiency of CO_2 assimilation). Our results demonstrated the variation of SIF-GPP relationship within C4 crops and highlighted the importance of leaf physiology including energy partitioning and leaf biochemical limitations in determining the canopy SIF behaviors as well as canopy SIF-GPP relationships under various environmental conditions. Future work should consider the species differences within each PFT in terms of canopy structure, leaf physiology and phenology to advance our mechanistic understanding of the relationship between SIF and GPP.

Declaration of Competing Interest

The authors declare that they have no known competing financial interests or personal relationships that could have appeared to influence the work reported in this paper.

Acknowledgements

This work was funded by the DOE Center for Advanced Bioenergy and Bioproducts Innovation (U.S. Department of Energy, Office of Science, Office of Biological and Environmental Research under Award Number DE-SC0018420). Any opinions, findings, and conclusions or recommendations expressed in this publication are those of the author (s) and do not necessarily reflect the views of the U.S. Department of Energy. GW and KG also acknowledged the support from NASA Future Investigators in NASA Earth and Space Science and Technology (FINESST) Program. GW, KG, and HK, acknowledged the support from NASA Carbon Monitoring System program managed by the NASA Terrestrial Ecology Program. We thank M. Pilar Cendrero-Mateo for sharing the iFLD code for SIF retrieval.

Supplementary materials

Supplementary material associated with this article can be found, in the online version, at doi:10.1016/j.agrformet.2022.109046.

Appendix A. The diurnal pattern of SIF_{760}, GPP, SIFy, LUE, $\Phi_{F,\ Canopy}$ and f_{esc} on normal and high VPD days

(Figs. A1–A3)

References

Ač, A., Malenovský, Z., Olejníčková, J., Gallé, A., Rascher, U., Mohammed, G., 2015. Meta-analysis assessing potential of steady-state chlorophyll fluorescence for remote sensing detection of plant water, temperature and nitrogen stress. Remote Sens. Environ. 168, 420–436.

Alonso, L., Gomez-Chova, L., Vila-Frances, J., Amoros-Lopez, J., Guanter, L., Calpe, J., Moreno, J., 2008. Improved fraunhofer line discrimination method for vegetation fluorescence quantification. IEEE Geosci. Remote Sens. Lett. 5, 620–624.

Baker, N.R., 2008. Chlorophyll fluorescence: a probe of photosynthesis in vivo. Annu. Rev. Plant Biol. 59, 89–113.

Baret, F., Guyot, G., 1991. Potentials and limits of vegetation indices for LAI and APAR assessment. Remote Sens. Lett. 35, 161–173.

Beale, C.V., Long, S.P., 1995. Can perennial C4 grasses attain high efficiencies of radiant energy conversion in cool climates? Plant Cell Environ. 18, 641–650.

Celesti, M., van der Tol, C., Cogliati, S., Panigada, C., Yang, P., Pinto, F., Rascher, U., Miglietta, F., Colombo, R., Rossini, M., 2018. Exploring the physiological information of Sun-induced chlorophyll fluorescence through radiative transfer model inversion. Remote Sens. Environ. 215, 97–108.

Cendrero-Mateo, M.P., Wieneke, S., Damm, A., Alonso, L., Pinto, F., Moreno, J., Guanter, L., Celesti, M., Rossini, M., Sabater, N., et al., 2019. Sun-induced chlorophyll fluorescence III: benchmarking retrieval methods and sensor characteristics for proximal sensing. Remote Sens. 11, 962.

Chang, C.Y., Wen, J., Han, J., Kira, O., Levonne, J., Melkonian, J., Riha, S.J., Skovira, J., Ng, S., Gu, L., et al., 2021. Unpacking the drivers of diurnal dynamics of sun-induced chlorophyll fluorescence (SIF): canopy structure, plant physiology, instrument configuration and retrieval methods. Remote Sens. Environ. 265, 112672.

Chen, B., Black, T.A., Coops, N.C., Hilker, T., Trofymow, J.A., Morgenstern, K., 2009. Assessing tower flux footprint climatology and scaling between remotely sensed and eddy covariance measurements. Bound. Layer Meteorol. 130, 137–167.

Chen, A., Mao, J., Ricciuto, D., Lu, D., Xiao, J., Li, X., Thornton, P.E., Knapp, A.K., 2021a. Seasonal changes in GPP/SIF ratios and their climatic determinants across the Northern Hemisphere. Global Change Biol. 27, 5186–5197.

Chen, A., Mao, J., Ricciuto, D., Xiao, J., Frankenberg, C., Li, X., Thornton, P.E., Gu, L., Knapp, AK., 2021b. Moisture availability mediates the relationship between terrestrial gross primary production and solar-induced chlorophyll fluorescence: insights from global-scale variations. Global Change Biol. 27, 1144–1156.

Chou, S., Chen, J.M., Yu, H., Chen, B., Zhang, X., Croft, H., Khalid, S., Li, M., Shi, Q., 2017. Canopy-level photochemical reflectance index from hyperspectral remote sensing and leaf-level non-photochemical quenching as early indicators of water stress in maize. Remote Sens. 9, 1–17.

Damm, A., Guanter, L., Paul-Limoges, E., van der Tol, C., Hueni, A., Buchmann, N., Eugster, W., Ammann, C., Schaepman, M.E., 2015. Far-red sun-induced chlorophyll fluorescence shows ecosystem-specific relationships to gross primary production: an assessment based on observational and modeling approaches. Remote Sens. Environ. 166, 91–105.

Dechant, B., Ryu, Y., Badgley, G., Köhler, P., Rascher, U., Migliavacca, M., Zhang, Y., Tagliabue, G., Guan, K., Rossini, M., et al., 2022. NIRVP: a robust structural proxy for sun-induced chlorophyll fluorescence and photosynthesis across scales. Remote Sens. Environ. 268, 112763.

Dechant, B., Ryu, Y., Badgley, G., Zeng, Y., Berry, J.A., Zhang, Y., Goulas, Y., Li, Z., Zhang, Q., Kang, M., et al., 2020. Canopy structure explains the relationship between photosynthesis and sun-induced chlorophyll fluorescence in crops. Remote Sens. Environ. 241, 111733.

Dohleman, F.G., Long, S.P., 2009. More productive than maize in the Midwest: how does Miscanthus do it? Plant Physiol. 150, 2104–2115.

Felten, D., Fröba, N., Fries, J., Emmerling, C., 2013. Energy balances and greenhouse gas-mitigation potentials of bioenergy cropping systems (Miscanthus, rapeseed, and maize) based on farming conditions in Western Germany. Renew. Energy 55, 160–174.

Flexas, J., Escalona, J.M., Evain, S., Gulías, J., Moya, I., Osmond, C.B., Medrano, H., 2002. Steady-state chlorophyll fluorescence (Fs) measurements as a tool to follow variations of net CO2 assimilation and stomatal conductance during water-stress in C3 plants. Eur. Space Agency SP, 26–29 (Special Publication) ESA.

Flexas, J., Medrano, H., 2002. Drought-inhibition of photosynthesis in C3 plants: stomatal and non-stomatal limitations revisited. Ann. Bot. 89, 183–189.

Frankenberg, C., Berry, J., 2018. Solar Induced Chlorophyll Fluorescence: Origins, Relation to Photosynthesis and Retrieval. Elsevier.

Frankenberg, C., Fisher, J.B., Worden, J., Badgley, G., Saatchi, S.S., Lee, J.E., Toon, G.C., Butz, A., Jung, M., Kuze, A., et al., 2011. New global observations of the terrestrial carbon cycle from GOSAT: Patterns of plant fluorescence with gross primary productivity. Geophys. Res. Lett. 38, 1–22.

Gallo, K.P., Daughtry, C.S.T., Bauer, M.E., 1985. Spectral estimation of absorbed photosynthetically active radiation in corn canopies. Remote Sens. Environ. 17, 221–232.

Genty, B., Briantais, J.M., Baker, NR., 1989. The relationship between the quantum yield of photosynthetic electron transport and quenching of chlorophyll fluorescence. Bioch. Biophys. Acta 990, 87–92.

Goulas, Y., Fournier, A., Daumard, F., Champagne, S., Ounis, A., Marloie, O., Moya, I., 2017. Gross primary production of a wheat canopy relates stronger to far red than to red solar-induced chlorophyll fluorescence. Remote Sens. 9, 97.

Gu, L., Han, J., Wood, J.D., Chang, C.Y.Y., Sun, Y., 2019a. Sun-induced Chl fluorescence and its importance for biophysical modeling of photosynthesis based on light reactions. New Phytol. 223, 1179–1191.

Gu, L., Wood, J.D., Chang, C.-Y., Sun, Y., Riggs, J.S., 2019b. Advancing terrestrial ecosystem science with a novel automated measurement system for sun-induced chlorophyll fluorescence for integration with eddy covariance flux networks. J. Geophys. Res. 124, 127–146.

Guanter, L., Zhang, Y., Jung, M., Joiner, J., Voigt, M., Berry, J.A., Frankenberg, C., Huete, A.R., Zarco-Tejada, P., Lee, J.E.J.-E., et al., 2014. Global and time-resolved monitoring of crop photosynthesis with chlorophyll fluorescence. Proc. Natl. Acad. Sci. 111, E1327–E1333.

Hao, D., Asrar, G.R., Zeng, Y., Yang, X., Li, X., Xiao, J., Guan, K., Wen, J., Xiao, Q., Berry, J.A., et al., 2021. Potential of hotspot solar-induced chlorophyll fluorescence for better tracking terrestrial photosynthesis. Glob. Change Biol. 27, 2144–2158.

He, L., Chen, J.M., Liu, J., Mo, G., Joiner, J., 2017. Angular normalization of GOME-2 Sun-induced chlorophyll fluorescence observation as a better proxy of vegetation productivity. Geophys. Res. Lett. 44, 5691–5699.

He, L., Chen, J.M., Liu, J., Zheng, T., Wang, R., Joiner, J., Chou, S., Chen, B., Liu, Y., Liu, R., et al., 2019. Diverse photosynthetic capacity of global ecosystems mapped by satellite chlorophyll fluorescence measurements. Remote Sens. Environ. 232, 111344.

He, L., Magney, T., Dutta, D., Yin, Y., Köhler, P., Grossmann, K., Stutz, J., Dold, C., Hatfield, J., Guan, K., et al., 2020. From the ground to space: using solar-induced chlorophyll fluorescence (SIF) to estimate crop productivity. Geophys. Res. Lett. 47, 1–12.

Heaton, E.A., Dohleman, F.G., Miguez, A.F., Juvik, J.A., Lozovaya, V., Widholm, J., Zabotina, O.A., McIsaac, G.F., David, M.B., Voigt, T.B., et al., 2010. Miscanthus. Advances in Botanical Research. A Promising Biomass Crop, pp. 75–137.

Hendrickson, L., Furbank, R.T., Chow, WS., 2004. A simple alternative approach to assessing the fate of absorbed light energy using chlorophyll fluorescence. Photosynth. Res. 82, 73–81.

Hsieh, C.I., Katul, G., Chi, TW., 2000. An approximate analytical model for footprint estimation of scalar fluxes in thermally stratified atmospheric flows. Adv. Water Res. 23, 765–772.

Illinois State Water Survey, 2020. Water and Atmospheric Resources Monitoring Program. Climate Network, Illinois.

Jiang, C., Guan, K., Wu, G., Peng, B., Wang, S.. 2020. A daily, 250 m, and real-time gross primary productivity product (2000 – present) covering the Contiguous United States. Earth System Science Data 1786.

Jifon, J.L., Syvertsen, JP., 2003. Erratum: Moderate shade can increase net gas exchange and reduce photoinhibition in citrus leaves (Tree Physiology 22 (1079-1092)). Tree Physiol. 23, 719.

Keenan, T.F., Migliavacca, M., Papale, D., Baldocchi, D., Reichstein, M., Torn, M., Wutzler, T., 2019. Widespread inhibition of daytime ecosystem respiration. Nat. Ecol. Evol. 3, 407–415.

Kim, J., Ryu, Y., Dechant, B., Lee, H., Kim, H., Kornfeld, A., Berry, JA., 2021. Solar-induced chlorophyll fluorescence is nonlinearly related to canopy photosynthesis in a temperate evergreen needleleaf forest. Remote Sens. Environ. 258, 112362.

Kimm, H., Guan, K., Jiang, C., Miao, G., Wu, G., Suyker, A.E., Ainsworth, E.A., Bernacchi, C.J., Montes, C.M., Berry, J.A., et al., 2021. A physiological signal derived from sun-induced chlorophyll fluorescence quantifies crop physiological response to environmental stresses in the U.S. Corn Belt. Environ. Res. Lett. 16, 124051.

Kira, O., Chang C, Y-Y., Gu, L., Wen, J., Hong, Z., Sun, Y., 2021. Partitioning net ecosystem exchange (NEE) of CO2 using solar-induced chlorophyll fluorescence (SIF). Geophys. Res. Lett. 48, e2020GL091247.

Kljun, N., Calanca, P., Rotach, M.W., Schmid, HP., 2015. A simple two-dimensional parameterisation for flux footprint prediction (FFP). Geosci. Model Dev 8, 3695–3713.

Kooijmans, L.M.J., Sun, W., Aalto, J., Erkkilä, K.M., Maseyk, K., Seibt, U., Vesala, T., Mammarella, I., Chen, H., 2019. Influences of light and humidity on carbonyl sulfide-based estimates of photosynthesis. Proc. Nat. Acad. Sci. U.S.A. 116, 2470–2475.

Lasslop, G., Reichstein, M., Papale, D., Richardson, A., Arneth, A., Barr, A., Stoy, P., Wohlfahrt, G., 2010. Separation of net ecosystem exchange into assimilation and respiration using a light response curve approach: critical issues and global evaluation. Global Change Biol. 16, 187–208.

Lee, M., Wycislo, A., Guo, J., Lee, D.K., Voigt, T., 2017. Nitrogen fertilization effects on biomass production and yield components of miscanthus ×giganteus. Front. Plant Sci. 8, 544.

Li, X., Xiao, J., 2019. Mapping photosynthesis solely from solar-induced chlorophyll fluorescence: a global, fine-resolution dataset of gross primary production derived from OCO-2. Remote Sensing 11, 2563.

Li, X., Xiao, J., 2022. TROPOMI observations allow for robust exploration of the relationship between solar-induced chlorophyll fluorescence and terrestrial gross primary production. Remote Sens. Environ. 268, 112748.

Li, Z., Zhang, Q., Li, J., Yang, X., Wu, Y., Zhang, Z., Wang, S., Wang, H., Zhang, Y., 2020. Solar-induced chlorophyll fluorescence and its link to canopy photosynthesis in maize from continuous ground measurements. Remote Sens. Environ. 236, 111420.

Liu, Y., Chen, J.M., He, L., Zhang, Z., Wang, R., Rogers, C., Fan, W., de Oliveira, G., Xie, X., 2022a. Non-linearity between gross primary productivity and far-red solar-induced chlorophyll fluorescence emitted from canopies of major biomes. Remote Sens. Environ. 271, 112896.

Liu, Y., Chen, J.M., He, L., Zhang, Z., Wang, R., Rogers, C., Fan, W., de Oliveira, G., Xie, X., 2022b. Non-linearity between gross primary productivity and far-red solar-induced chlorophyll fluorescence emitted from canopies of major biomes. Remote Sens. Environ. 271, 112896.

Liu, X., Liu, L., Hu, J., Du, S., 2017. Modeling the footprint and equivalent radiance transfer path length for tower-based hemispherical observations of chlorophyll fluorescence. Sensors 17, 1–15.

MacBean, N., Maignan, F., Bacour, C., Lewis, P., Peylin, P., Guanter, L., Köhler, P., Gómez-Dans, J., Disney, M., 2018. Strong constraint on modelled global carbon uptake using solar-induced chlorophyll fluorescence data. Sci. Rep. 8, 1–12.
Magney, T.S., Bowling, D.R., Logan, B.A., Grossmann, K., Stutz, J., Blanken, P.D., Burns, S.P., Cheng, R., Garcia, M.A., Köhler, P., et al., 2019. Mechanistic evidence for tracking the seasonality of photosynthesis with solar-induced fluorescence. Proc. Nat. Acad. Sci. U.S.A. 116, 11640–11645.
Miao, G., Guan, K., Suyker, A.E., Yang, X., Arkebauer, T.J., Walter-Shea, E.A., Kimm, H., Hmimina, G.Y., Gamon, J.A., Franz, T.E., et al., 2020. Varying contributions of drivers to the relationship between canopy photosynthesis and far-red sun-induced fluorescence for two maize sites at different temporal scales. J. Geophys. Res. 125, 1–17.
Miao, G., Guan, K., Yang, X., Bernacchi, C.J., Berry, J.A., DeLucia, E.H., Wu, J., Moore, C. E., Meacham, K., Cai, Y., et al., 2018. Sun-induced chlorophyll fluorescence, photosynthesis, and light use efficiency of a soybean field from seasonally continuous measurements. J. Geophys. Res. 123, 610–623.
Migliavacca, M., Perez-Priego, O., Rossini, M., El-Madany, T.S., Moreno, G., van der Tol, C., Rascher, U., Berninger, A., Bessenbacher, V., Burkart, A., et al., 2017. Plant functional traits and canopy structure control the relationship between photosynthetic CO2uptake and far-red sun-induced fluorescence in a Mediterranean grassland under different nutrient availability. New Phytol. 214, 1078–1091.
Mohammed, G.H., Colombo, R., Middleton, E.M., Rascher, U., van der Tol, C., Nedbal, L., Goulas, Y., Pérez-Priego, O., Damm, A., Meroni, M., et al., 2019. Remote sensing of solar-induced chlorophyll fluorescence (SIF) in vegetation: 50 years of progress. Remote Sens. Environ. 231, 111177.
Monteith, J.L., 1972. Solar radiation and productivity in tropical ecosystems. J. Appl. Ecol. 9, 747–766.
Moore, C.E., von Haden, A.C., Burnham, M.B., Kantola, I.B., Gibson, C.D., Blakely, B.J., Dracup, E.C., Masters, M.D., Yang, W.H., DeLucia, E.H., et al., 2021. Ecosystem-scale biogeochemical fluxes from three bioenergy crop candidates: how energy sorghum compares to maize and miscanthus. GCB Bioenergy 13, 445–458.
Müller, P., Li, X.P., Niyogi, K.K., 2001. Non-photochemical quenching . a response to excess light energy. Plant Physiol. 125, 1558–1566.
Mumm, R.H., Goldsmith, P.D., Rausch, K.D., Stein, H.H., 2015. Land usage attributed to corn ethanol production in the united states: sensitivity to technological advances in corn grain yield, ethanol conversion, and co-product utilization. Biotechnol. Biofuels 7, 61.
Naidu, S.L., Long, SP., 2004. Potential mechanisms of low-temperature tolerance of C4 photosynthesis in Miscanthus x giganteus: an in vivo analysis. Planta 220, 145–155.
Norton, A.J., Rayner, P.J., Koffi, E.N., Scholze, M., Silver, J.D., Wang, Y.-P., 2019. Estimating global gross primary productivity using chlorophyll fluorescence and a data assimilation system with the BETHY-SCOPE model. Biogeosciences 16, 3069–3093.
Pastorello, G., Trotta, C., Canfora, E., Chu, H., Christianson, D., Cheah, Y.W., Poindexter, C., Chen, J., Elbashandy, A., Humphrey, M., et al., 2020. The FLUXNET2015 dataset and the ONEFlux processing pipeline for eddy covariance data. Sci. Data 7, 225.
Paul-Limoges, E., Damm, A., Hueni, A., Liebisch, F., Eugster, W., Schaepman, M.E., Buchmann, N., 2018. Effect of environmental conditions on sun-induced fluorescence in a mixed forest and a cropland. Remote Sens. Environ. 219, 310–323.
Peguero-Pina, J.J., Morales, F., Flexas, J., Gil-Pelegrín, E., Moya, I., 2008. Photochemistry, remotely sensed physiological reflectance index and de-epoxidation state of the xanthophyll cycle in Quercus coccifera under intense drought. Oecologia 156, 1–11.
Porcar-Castell, A., Malenovský, Z., Magney, T., Van Wittenberghe, S., Fernández-Marín, B., Maignan, F., Zhang, Y., Maseyk, K., Atherton, J., Albert, L.P., et al., 2021. Chlorophyll a fluorescence illuminates a path connecting plant molecular biology to Earth-system science. Nat. Plants 7, 998–1009.
Porcar-Castell, A., Tyystjärvi, E., Atherton, J., Van Der Tol, C., Flexas, J., Pfündel, E.E., Moreno, J., Frankenberg, C., Berry, JA., 2014. Linking chlorophyll a fluorescence to photosynthesis for remote sensing applications: mechanisms and challenges. J. Exp. Bot. 65, 4065–4095.
De Pury, G.G., Farquhar, GD., 1997. Simple scaling of photosynthesis from leaves to canopies without the errors of big-leaf models. Plant Cell Environ. 20, 537–557.
Reichstein, M., Falge, E., Baldocchi, D., Papale, D., Aubinet, M., Berbigier, P., Bernhofer, C., Buchmann, N., Gilmanov, T., Granier, A., et al., 2005. On the separation of net ecosystem exchange into assimilation and ecosystem respiration: review and improved algorithm. Global Change Biol. 11, 1424–1439.
Retkute, R., Townsend, A.J., Murchie, E.H., Jensen, O.E., Preston, SP., 2018. Three-dimensional plant architecture and sunlit-shaded patterns: a stochastic model of light dynamics in canopies. Ann. Bot. 122, 291–302.
Robertson, G.P., Hamilton, S.K., Barham, B.L., Dale, B.E., Izaurralde, R.C., Jackson, R.D., Landis, D.A., Swinton, S.M., Thelen, K.D., Tiedje, JM., 2017. Cellulosic biofuel contributions to a sustainable energy future: choices and outcomes. Science 356, eaal2324.
Romero, J.M., Cordon, G.B., Lagorio, MG., 2018. Modeling re-absorption of fluorescence from the leaf to the canopy level. Remote Sens. Environ. 204, 138–146.
Ryu, Y., Berry, J.A., Baldocchi, DD., 2019. What is global photosynthesis? History, uncertainties and opportunities. Remote Sens. Environ. 223, 95–114.
Smith, C.M., David, M.B., Mitchell, C.A., Masters, M.D., Anderson-Teixeira, K.J., Bernacchi, C.J., DeLucia, E.H., 2013. Reduced nitrogen losses after conversion of row crop agriculture to perennial biofuel crops. J. Environ. Qual. 42, 219–228.
Stinecipher, J.R., Cameron-Smith, P., Kuai, L., Glatthor, N., Höpfner, M., Baker, I., Beer, C., Bowman, K., Lee, M., Miller, S.M., et al., 2022. Remotely sensed carbonyl sulfide constrains model estimates of amazon primary productivity. Geophys. Res. Lett. 49, e2021GL096802.
Sun, Y., Frankenberg, C., Wood, J.D., Schimel, D.S., Jung, M., Guanter, L., Drewry, D.T., Verma, M., Porcar-Castell, A., Griffis, T.J., et al., 2017. OCO-2 advances photosynthesis observation from space via solar-induced chlorophyll fluorescence. Science 358, eaam5747.
Thum, T., Zaehle, S., Köhler, P., Aalto, T., Aurela, M., Guanter, L., Kolari, P., Laurila, T., Lohila, A., Magnani, F., 2017. Modelling sun-induced fluorescence and photosynthesis with a land surface model at local and regional scales in northern Europe. Biogeosciences 14, 1969–1984.
Van Der Tol, C., Berry, J.A., Campbell, P.K.E., Rascher, U., 2014. Models of fluorescence and photosynthesis for interpreting measurements of solar-induced chlorophyll fluorescence. J. Geophys. Res. 119, 2312–2327.
Verma, M., Schimel, D., Evans, B., Frankenberg, C., Beringer, J., Drewry, D.T., Magney, T., Marang, I., Hutley, L., Moore, C., et al., 2017. Effect of environmental conditions on the relationship between solar-induced fluorescence and gross primary productivity at an OzFlux grassland site. J. Geophys. Res. 122, 716–733.
Vickers, D., Mahrt, L., 1997. Quality control and flux sampling problems for tower and aircraft data. J. Atmos. Oceanic Technol. 14, 512–526.
Viña, A., Gitelson, AA., 2005. New developments in the remote estimation of the fraction of absorbed photosynthetically active radiation in crops. Geophys. Res. Lett. 32, 1–4.
Wang, X., Chen, J.M., Ju, W., 2020. Photochemical reflectance index (PRI) can be used to improve the relationship between gross primary productivity (GPP) and sun-induced chlorophyll fluorescence (SIF). Remote Sens. Environ. 246, 111888.
Webb, E.K., Pearman, G.I., Leuning, R., 1980. Correction of flux measurements for density effects due to heat and water vapour transfer. Q. J. R. Meteorolog. Soc. 106, 85–100.
Wehr, R., Munger, W., Mcmanus, B., Nelson, D.D., Zahniser, M.S., Davidson, E.A., Wofsy, S.C., Saleska, S.R., 2016. Seasonality of temperate forest photosynthesis and daytime respiration. Nature 534, 680–683.
Weiss, A., Norman, J.M.M., 1985. Partitioning solar radiation into direct and diffuse, visible and near-infrared components. Agric. For. Meteorol. 34, 205–213.
Wen, J., Köhler, P., Duveiller, G., Parazoo, N.C., Magney, T.S., Hooker, G., Yu, L., Chang, C.Y., Sun, Y., 2020. A framework for harmonizing multiple satellite instruments to generate a long-term global high spatial-resolution solar-induced chlorophyll fluorescence (SIF). Remote Sens. Environ. 239, 111644.
Wu, G., Guan, K., Jiang, C., Peng, B., Kimm, H., Chen, M., Yang, X., Wang, S., Suyker, A. E., Bernacchi, C.J., et al., 2020. Radiance-based NIRv as a proxy for GPP of corn and soybean. Environ. Res. Lett. 15, 034009.
Yang, K., Ryu, Y., Dechant, B., Berry, J.A., Hwang, Y., Jiang, C., Kang, M., Kim, J., Kimm, H., Kornfeld, A., et al., 2018a. Sun-induced chlorophyll fluorescence is more strongly related to absorbed light than to photosynthesis at half-hourly resolution in a rice paddy. Remote Sens. Environ. 216, 658–673.
Yang, X., Shi, H., Stovall, A., Guan, K., Miao, G., Zhang, Y., Zhang, Y., Xiao, X., Ryu, Y., Lee, J.E., 2018b. FluoSpec 2—an automated field spectroscopy system to monitor canopy solar-induced fluorescence. Sensors 18, 2063.
Yang, P., van der Tol, C., 2018. Linking canopy scattering of far-red sun-induced chlorophyll fluorescence with reflectance. Remote Sens. Environ. 209, 456–467.
Yang, P., van der Tol, C., Campbell, P.K.E., Middleton, EM., 2021. Unraveling the physical and physiological basis for the solar- induced chlorophyll fluorescence and photosynthesis relationship using continuous leaf and canopy measurements of a corn crop. Biogeosciences 18, 441–465.
Zeng, Y., Badgley, G., Dechant, B., Ryu, Y.Y., Chen, M., Berry, J., 2019. A practical approach for estimating the escape ratio of near-infrared solar-induced chlorophyll fluorescence. Remote Sens. Environ. 232, 111209.
Zhan, W., Yang, X., Ryu, Y., Dechant, B., Huang, Y., Goulas, Y., Kang, M., Gentine, P., 2022. Two for one: partitioning CO2 fluxes and understanding the relationship between solar-induced chlorophyll fluorescence and gross primary productivity using machine learning. Agric. For. Meteorol. 321, 108980.
Zhang, Q., Chen, J.M., Ju, W., Zhang, Y., Li, Z., He, L., Pacheco-Labrador, J., Li, J., Qiu, B., Zhang, X., et al., 2021. Ground-based multiangle solar-induced chlorophyll fluorescence observation and angular normalization for assessing crop productivity. J. Geophys. Res. 126, e2020JG006082.
Zhang, Y., Guanter, L., Berry, J.A., van der Tol, C., Yang, X., Tang, J., Zhang, F., 2016. Model-based analysis of the relationship between sun-induced chlorophyll fluorescence and gross primary production for remote sensing applications. Remote Sens. Environ. 187, 145–155.
Zhang, Z., Zhang, Y., Porcar-Castell, A., Joiner, J., Guanter, L., Yang, X., Migliavacca, M., Ju, W., Sun, Z., Chen, S., et al., 2020a. Reduction of structural impacts and distinction of photosynthetic pathways in a global estimation of GPP from space-borne solar-induced chlorophyll fluorescence. Remote Sens. Environ. 240, 111722.
Zhang, Z., Zhang, Y., Zhang, Y., Chen, JM., 2020b. Correcting clear-sky bias in gross primary production modeling from satellite solar-induced chlorophyll fluorescence data. J. Geophys. Res. 125, 1–16.
Zhou, H., Wu, D., Lin, Y., 2020. The relationship between solar-induced fluorescence and gross primary productivity under different growth conditions: global analysis using satellite and biogeochemical model data. Int. J. Remote Sens. 41, 7660–7679.